Study of $\tau \to eM^+M^-$ decays in N-B-LSSM*

Rong-Zhi Sun (孙荣智)[1,2,3] Shu-Min Zhao (赵树民)[1,2,3†] Shuang Di (邸爽)[1,2,3] Xing-Xing Dong (董幸幸)[1,2,3,4‡]

[1]Department of Physics, Hebei University, Baoding 071002, China
[2]Hebei Key Laboratory of High-precision Computation and Application of Quantum Field Theory, Baoding 071002, China
[3]Hebei Research Center of the Basic Discipline for Computational Physics, Baoding 071002, China
[4]Departamento de Fisica and CFTP, Instituto Superior Técnico, Universidade de Lisboa, Lisboa 1049-001, Portugal

Abstract: Within the framework of the next-to-minimal supersymmetric (SUSY) extension of the Standard Model (SM) with a local B-L gauge symmetry (N-B-LSSM), we study lepton flavor violating (LFV)$\tau \to eM^+M^-$ decays: $\tau \to e\pi^+\pi^-$, $\tau \to e\pi^+K^-$, and $\tau \to eK^+K^-$. Based on the latest experimental data, the influence of different sensitive parameters on the branching ratios is considered. It can be seen from the numerical analysis that the main sensitive parameters and LFV sources are non-diagonal elements corresponding to the initial and final leptons. This work can provide a basis for discovering the existence of new physics (NP).

Keywords: beyond standard model, supersymmetry, lepton flavor violation, new physics

DOI: 10.1088/1674-1137/adec4c **CSTR:** 32044.14.ChinesePhysicsC.49113110

I. INTRODUCTION

As the cornerstone of particle physics, the standard model (SM) has achieved significant success with the detection of the lightest CP-even Higgs [1−4]. Nevertheless, SM still faces several critical limitations in explaining fundamental phenomena. Firstly, because of the absence of right-handed neutrinos and the presence of only Yukawa couplings of quarks and charged leptons, SM predicts that neutrinos are strictly massless, which directly contradicts the neutrino oscillations revealed by the Super-Kamioka Neutrino Detection Experiment (1998) [5−8]. Secondly, no stable and non-electric new particles in the SM can explain the large number of dark matter components observed in the universe. In addition, there is a gauge hierarchy problem in SM, wherein there is a large difference between the weak energy scale $m_{\rm EW}$ and Planck energy scale $M_{\rm Pl}$. Moreover, because of the extremely small neutrino mixing angle and existence of the Glashow-Iliopoulos-Maiani (GIM) mechanism, LFV processes in the SM are highly suppressed, well below the detection sensitivity of the Belle II experiment. Furthermore, SM does not incorporate gravitational interaction. The Minimal Supersymmetric Standard Model (MSSM) is the minimal expansion of the SUSY theory to SM [9−11]. It can explain the hierarchy problem, ensure high-energy scale unification of the gauge coupling constants, and provide candidates for dark matter, partially compensating for the deficiencies of SM. However, the MSSM has not yet solved the μ problem or the neutrino mass problem.

Building on the MSSM, the N-B-LSSM extends the gauge group to $SU(3)_C \otimes SU(2)_L \otimes U(1)_Y \otimes U(1)_{B-L}$, where B and L denote baryon and lepton numbers, respectively (as first proposed in Ref. [12]). In this model, two Higgs singlets carrying opposite $B-L$ charges $\hat{\chi}_1$ and $\hat{\chi}_2$ are introduced to trigger the spontaneous breaking of the $U(1)_{B-L}$ symmetry; meanwhile, three generation right-handed neutrinos $\hat{\nu}_i$ acquire Majorana masses through coupling with $\hat{\chi}_1$, and the additional singlet $\hat{S}$ is used to solve the μ problem in the superpotential. Furthermore, under the N-B-LSSM model, lepton number violation and baryon number violation processes can also occur, which help explain the matter-antimatter asymmetry in the universe. Right-handed neutrinos generate tiny masses through the Type-I seesaw mechanism, consistent with neutrino oscillation experiments, and neutralinos (as the lightest MSSM particles) can exist as dark matter candid-

Received 23 May 2025; Accepted 4 July 2025; Published online 5 July 2025

* Supported by National Natural Science Foundation of China (NNSFC) (12075074), Natural Science Foundation of Hebei Province (A2023201040, A2022201022, A2022201017, A2023201041), Natural Science Foundation of Hebei Education Department (QN2022173), Post-graduate's Innovation Fund Project of Hebei University (HBU2024SS042), the Project of the China Scholarship Council (CSC) (202408130113). X. Dong acknowledges support from Fundação para a Ciência e a Tecnologia (FCT, Portugal) through the projects CFTP FCT Unit (UIDB/00777/2020, UIDP/00777/2020)

† E-mail: zhaosm@hbu.edu.cn
‡ E-mail: dongxx@hbu.edu.cn

ates. The superpotential includes a trilinear term $\lambda\hat{S}\hat{H}_u\hat{H}_d$; when $\hat{S}$ acquires a vacuum expectation value (VEV) $\frac{v_S}{\sqrt{2}}$, it induces an effective μ term $\mu = \lambda v_S/\sqrt{2}$, thereby naturally alleviating the μ problem of MSSM. The enlarged Higgs sector extends the neutral CP-even mass matrix to 5×5, offering greater flexibility to fit the observed 125.20 ± 0.11 GeV Higgs mass and predicting additional scalar states for future experimental exploration. Additionally, N-B-LSSM extends the gauge symmetry by introducing an extra $U(1)_{B-L}$ gauge group and its corresponding gauge boson B'^{μ}, along with two new gauge coupling constants g_B and g_{YB}. The associated gaugino $\tilde{B}'$, together with the Higgsinos $\tilde{\chi}_1$, $\tilde{\chi}_2$, and $\tilde{S}$, enlarge the neutralino mass matrix from 4×4 to 8×8. The introduction of right-handed neutrinos also doubles the dimensions of the sneutrino mass matrix from 3×3 to 6×6, significantly enriching the flavor structure. These extensions allow sizable LFV signals to arise even with mild flavor-mixing parameters, thereby enhancing the model's predictive power in the LFV processes. Moreover, R-parity is automatically conserved in N-B-LSSM owing to the extended gauge structure, defined by the relation $R_p = (-1)^{3(B-L)+2S}$, without requiring additional assumptions. Finally, high scale VEVs (v_η, $v_{\bar{\eta}}$, and v_S) alleviate the hierarchy problem by reducing the dependence on electroweak fine-tuning.

For comparison, the next-to-minimal supersymmetric standard model (NMSSM) introduces only one additional Higgs singlet superfield $\hat{S}$, with superpotential terms such as $\lambda\hat{H}_u\cdot\hat{H}_d\hat{S}$ and $\frac{1}{3}\kappa\hat{S}^3$, which also address the μ problem to some extent. However, it lacks neutrino mass generation mechanisms present in N-B-LSSM. As a result, its phenomenological impact on the LFV processes remains similar to that of MSSM. In summary, the choice to study the LFV processes within the N-B-LSSM framework is grounded in the model's multiple theoretical advantages, including the generation of neutrino masses, alleviation of the μ problem, a more flexible Higgs sector, automatic R-parity conservation, and a richer particle and flavor structure. These features make N-B-LSSM a more compelling platform for exploring LFV.

In the SM framework, the pion and kaon mesons play a critical role as pseudo-Goldstone bosons in low-energy quantum chromodynamics (QCD), being composed of a quark and an antiquark. The π^+ meson is constituted by an up quark (u) and an anti-down quark ($\bar{d}$), while the π^- meson is formed by a down quark (d) and an anti-up quark ($\bar{u}$). These two mesons belong to an isospin triplet, embodying the effective degrees of freedom emerging from the spontaneous breaking of chiral symmetry. By contrast, owing to the inclusion of a strange quark, the structure of the kaon mesons is more distinct: the K^+ meson is composed of an up quark (u) and an anti-strange quark ($\bar{s}$), while the K^- meson consists of a strange quark (s) and an anti-up quark ($\bar{u}$). As a consequence, the mass of the kaon is significantly higher than that of the pion, reflecting the effects of $SU(3)$ flavor symmetry and its explicit breaking. In N-B-LSSM, the processes in which a τ lepton decays to an electron plus a meson pair ($\tau\to e\pi^+\pi^-$, $\tau\to e\pi^+K^-$, $\tau\to eK^+K^-$) provide a sensitive platform for probing new physics (NP) effects.

Over the past few decades, LFV has become one of the core directions in exploring NP beyond the Standard Model (BSM). Owing to its largest mass and rich decay channels, τ lepton shows unique advantages in LFV searches. Ref. [13] investigates LFV in τ decays within a SUSY seesaw model. It reveals that scalar-mediated $\tau\to\ell f_0(980)$ and $\tau\to\ell K^+K^-$ branching ratios can reach $O(10^{-7})$, surpassing pseudoscalar channels $\tau\to\ell\eta^{(\prime)}$. Moreover, it links $\tau\to\ell\mu^+\mu^-$ to these processes, thereby identifying critical experimental targets for probing scalar-mediated LFV mechanisms. Ref. [14] studies semileptonic LFV τ decays $\tau\to\mu PP$, $\tau\to\mu P$, $\tau\to\mu V$ in CMSSM-seesaw and NUHM-seesaw frameworks via full one-loop analysis of γ-, Z- and Higgs-mediated contributions. It identifies discrepancies in predicted branching ratios for $\tau\to\mu\eta$, $\tau\to\mu\eta'$, and $\tau\to\mu K^+K^-$, proposing these channels as critical tests for LFV and Higgs-sector dynamics, with simplified formulas to aid experimental validation. Ref. [15] explores LFV $\tau\to\ell P(V)$ and $\tau\to 3\ell$ decays within the Type-III seesaw model. By constraining the parameter space via experimental limits from leptonic Z-boson decays, the study predicts branching ratios for these processes that align with current experimental upper bounds. Ref. [16] investigates LFV Higgs decays $h\to\tau\ell$ ($\ell = e, \mu$) and their connection to hadronic τ-decays (e.g., $\tau\to\ell\pi\pi$, $\tau\to\ell\eta^{(\prime)}$), aiming to distinguish scalar and pseudoscalar couplings in the Higgs sectors through low-energy processes, while improving the theoretical description of relevant hadronic matrix elements. Ref. [17] discusses the violation of lepton flavour universality (LFU) in B-decays by incorporating quantum corrections, such as a renormalization group equation (RGE) running from a high-energy scale Λ, and predicts potential signals in LFV processes like $\tau\to\mu\ell\ell$, $\tau\to\mu\rho$, $\tau\to\mu\pi$, $\tau\to\mu\eta^{(\prime)}$. Ref. [18] emphasizes that the Belle experiment has set upper limits on the branching ratios of τ LFV and lepton number violation (LNV) decays, and anticipates Belle II to further probe these τ LFV/LNV decays in the coming decades. With a 50-fold increase in statistics, Belle II may reach branching ratios of $O(10^{-7})-O(10^{-9})$ predicted by NP models, revealing possible signals of BSM. Ref. [19] studies LFV decays $\tau\to Pl(P=\pi,\eta,\eta';\ l=\mu,e)$ in the $U(1)_X$ SSM. By analyzing the impact of sensitive parameters using the latest experimental data on $\tau\to Pe$ and $\tau\to P\mu$, the study identifies non-diagonal elements as the primary sources of LFV, providing a theoretical foundation for exploring NP.

We investigate the LFV processes of τ to electron and

meson pairs within the framework of the N-B-LSSM model. Under the premise of fully considering the experimental limit of the $\tau \to e\gamma$ process [20], we derive the relevant Feynman diagrams and amplitudes, and conduct a detailed numerical analysis on the branching ratio of each process. During the analysis, the contributions of a variety of SUSY particles in the loop diagrams are considered separately, and the change trends of the various contributions are studied in different parameter ranges. The effects of different parameters on the branching ratios are shown through graphical results, the feasible parameter regions that satisfy the experimental limits are identified, and the key parameters that have a greater impact on the results are analyzed. The latest upper limits on the LFV branching ratios of $\tau \to e\pi^+\pi^-$, $\tau \to e\pi^+K^-$, and $\tau \to eK^+K^-$ at 90% confidence level (C.L.) [21] are

$$\begin{aligned}&\mathrm{BR}(\tau \to e\pi^+\pi^-) < 2.3\times10^{-8},\\&\mathrm{BR}(\tau \to e\pi^+K^-) < 3.7\times10^{-8},\\&\mathrm{BR}(\tau \to eK^+K^-) < 3.4\times10^{-8}.\end{aligned} \tag{1}$$

The paper is organized as follows. In Sec. II, we introduce the main content of N-B-LSSM, presenting the required mass matrices and corresponding couplings. In Sec. III, we derive analytical formulas for the branching ratios of the LFV processes $\tau \to e\pi^+\pi^-$, $\tau \to e\pi^+K^-$, and $\tau \to eK^+K^-$. In Sec. IV, we determine the input parameters and perform numerical analyses. In Sec. V, we summarize the conclusion of this study. Finally, in Appendix A, we gather some specific forms of Wilson coefficients required herein.

II. MAIN CONTENT OF N-B-LSSM

N-B-LSSM extends the local gauge group of MSSM to $SU(3)_C \otimes SU(2)_L \otimes U(1)_Y \otimes U(1)_{B-L}$. N-B-LSSM has new superfields beyond MSSM, including right-handed neutrinos $\hat{\nu}_i$ and three Higgs singlets $\hat{\chi}_1$, $\hat{\chi}_2$, and $\hat{S}$. Through the Type-I seesaw mechanism, the light neutrinos obtain a tiny mass at the tree level. Meanwhile, in the Higgs scalar part, the neutral CP-even components from H_u, H_d, χ_1, χ_2, and S are mixed to form a 5×5 mass squared matrix. When the loop corrections of SUSY particles are combined, the lightest CP-even Higgs mass can be modified to 125.20 ± 0.11 GeV [22, 23]. Furthermore, the sneutrinos are dispersed into CP-even sneutrinos and CP-odd sneutrinos, and their mass squared matrices are both extended to 6×6.

The superpotential in the N-B-LSSM is expressed as

$$\begin{aligned}W =& -Y_d\hat{d}\hat{q}\hat{H}_d - Y_e\hat{e}\hat{l}\hat{H}_d - \lambda_2\hat{S}\hat{\chi}_1\hat{\chi}_2 + \lambda\hat{S}\hat{H}_u\hat{H}_d\\&+\frac{\kappa}{3}\hat{S}\hat{S}\hat{S} + Y_u\hat{u}\hat{q}\hat{H}_u + Y_\chi\hat{\nu}\hat{\chi}_1\hat{\nu} + Y_\nu\hat{\nu}\hat{l}\hat{H}_u.\end{aligned} \tag{2}$$

The explicit forms of the two Higgs doublets are as follows:

$$\begin{aligned}H_u &= \begin{pmatrix} H_u^+ \\ \frac{1}{\sqrt{2}}\left(v_u + H_u^0 + iP_u^0\right)\end{pmatrix},\\H_d &= \begin{pmatrix} \frac{1}{\sqrt{2}}\left(v_d + H_d^0 + iP_d^0\right) \\ H_d^-\end{pmatrix}.\end{aligned} \tag{3}$$

The three Higgs singlets are represented by

$$\begin{aligned}\chi_1 &= \frac{1}{\sqrt{2}}\left(v_\eta + \phi_1^0 + iP_1^0\right),\\\chi_2 &= \frac{1}{\sqrt{2}}\left(v_{\bar{\eta}} + \phi_2^0 + iP_2^0\right),\\S &= \frac{1}{\sqrt{2}}\left(v_S + \phi_S^0 + iP_S^0\right).\end{aligned} \tag{4}$$

The VEVs of the Higgs superfields H_u, H_d, χ_1, χ_2, and S are denoted by v_u, v_d, v_η, $v_{\bar{\eta}}$, and v_S, respectively. Two angles are defined as $\tan\beta = v_u/v_d$ and $\tan\beta_\eta = v_{\bar{\eta}}/v_\eta$.

The soft SUSY breaking terms of N-B-LSSM are

$$\begin{aligned}\mathcal{L}_{\text{soft}} =& \mathcal{L}_{\text{soft}}^{MSSM} - \frac{T_\kappa}{3}S^3 + \epsilon_{ij}T_\lambda S H_d^i H_u^j + T_2 S\chi_1\chi_2\\&- T_{\chi,ik}\chi_1\tilde{\nu}_{R,i}^*\tilde{\nu}_{R,k}^* + \epsilon_{ij}T_{\nu,ij}H_u^i\tilde{\nu}_{R,i}^*\tilde{e}_{L,j} - m_\eta^2|\chi_1|^2 - m_{\bar{\eta}}^2|\chi_2|^2\\&- m_S^2|S|^2 - m_{\nu,ij}^2\tilde{\nu}_{R,i}^*\tilde{\nu}_{R,j} - \frac{1}{2}(2M_{BB'}\lambda_{\tilde{B}}\tilde{B}' + M_{BL}\tilde{B}'^2)\\&+\text{h.c.}.\end{aligned} \tag{5}$$

The particle contents and charge assignments for N-B-LSSM are shown in Table 1.

Table 1. Superfields in N-B-LSSM.

Superfields	$SU(3)_C$	$SU(2)_L$	$U(1)_Y$	$U(1)_{B-L}$
$\hat{q}$	3	2	1/6	1/6
$\hat{l}$	1	2	-1/2	-1/2
$\hat{H}_d$	1	2	-1/2	0
$\hat{H}_u$	1	2	1/2	0
$\hat{d}$	$\bar{3}$	1	1/3	-1/6
$\hat{u}$	$\bar{3}$	1	-2/3	-1/6
$\hat{e}$	1	1	1	1/2
$\hat{\nu}$	1	1	0	1/2
$\hat{\chi}_1$	1	1	0	-1
$\hat{\chi}_2$	1	1	0	1
$\hat{S}$	1	1	0	0

In the theory with two Abelian groups $U(1)_Y$ and $U(1)_{B-L}$, a new effect called gauge kinetic mixing occurs. Even if the initial value of this mixing term is zero at $M_{\rm GUT}$, non-zero values can still be generated through the evolution of RGEs.

The covariant derivatives of N-B-LSSM can be written as [24–27]

$$D_\mu = \partial_\mu - i\begin{pmatrix} Y^Y, & Y^{B-L} \end{pmatrix}\begin{pmatrix} g_Y, & g'_{YB} \\ g'_{BY}, & g'_{B-L} \end{pmatrix}\begin{pmatrix} B'^Y_\mu \\ B'^{BL}_\mu \end{pmatrix}. \tag{6}$$

B'^Y_μ and B'^{BL}_μ denote the gauge fields of $U(1)_Y$ and $U(1)_{B-L}$, respectively. Under the condition that the two Abelian gauge groups are not broken, we can do a change of basis using the rotation matrix R satisfying the orthogonality condition $R^TR = 1$ [24, 26, 27]:

$$\begin{pmatrix} g_Y, & g'_{YB} \\ g'_{BY}, & g'_{B-L} \end{pmatrix} R^T = \begin{pmatrix} g_1, & g_{YB} \\ 0, & g_B \end{pmatrix} \quad \text{and}$$
$$R\begin{pmatrix} B'^Y_\mu \\ B'^{BL}_\mu \end{pmatrix} = \begin{pmatrix} B^Y_\mu \\ B^{BL}_\mu \end{pmatrix}. \tag{7}$$

At the tree level, three neutral gauge bosons B^Y_μ, B^{BL}_μ, and V^3_μ undergo mixing, with their mass matrix expressed in the basis $(B^Y_\mu, B^{BL}_\mu, V^3_\mu)$:

$$\begin{pmatrix} \frac{1}{8}g_1^2v^2 & -\frac{1}{8}g_1g_2v^2 & \frac{1}{8}g_1(g_{YB}+g_B)v^2 \\ -\frac{1}{8}g_1g_2v^2 & \frac{1}{8}g_2^2v^2 & -\frac{1}{8}g_2(g_{YB}+g_B)v^2 \\ \frac{1}{8}g_1(g_{YB}+g_B)v^2 & -\frac{1}{8}g_2(g_{YB}+g_B)v^2 & \frac{1}{8}(g_{YB}+g_B)^2v^2+\frac{1}{8}g_B^2\xi^2 \end{pmatrix}, \tag{8}$$

with $v^2 = v_u^2 + v_d^2$ and $\xi^2 = v_\eta^2 + v_{\bar\eta}^2$.

The mass eigenvalues of the matrix in Eq. (8) are determined by two mixing angles: the Weinberg angle θ_W and a newly introduced angle θ'_W. The latter is defined as follows:

$$\sin^2\theta'_W = \frac{1}{2} - \frac{[(g_{YB}+g_B)^2 - g_1^2 - g_2^2]v^2 + 4g_B^2\xi^2}{2\sqrt{[(g_{YB}+g_B)^2+g_1^2+g_2^2]^2v^4 + 8g_B^2[(g_{YB}+g_B)^2 - g_1^2 - g_2^2]v^2\xi^2 + 16g_B^4\xi^4}}. \tag{9}$$

The new mixing angle appears in the couplings involving Z and Z'. The exact eigenvalues of Eq. (8) are deduced:

$$\begin{aligned} &m_\gamma^2 = 0, \\ &m_{Z,Z'}^2 = \frac{1}{8}\Big([g_1^2+g_2^2+(g_{YB}+g_B)^2]v^2 + 4g_B^2\xi^2 \mp \sqrt{[g_1^2+g_2^2+(g_{YB}+g_B)^2]^2v^4 + 8[(g_{YB}+g_B)^2 - g_1^2 - g_2^2]g_B^2v^2\xi^2 + 16g_B^4\xi^4}\Big). \end{aligned} \tag{10}$$

In the calculation, the mass squared matrices of the neutralino, chargino, slepton, CP-even sneutrino, CP-odd sneutrino, up squark, and down squark are required. These mass matrices can be found in Refs. [12, 20].

Here, we show some needed couplings in this model. The Z bosons interact with sneutrinos, whose explicit form reads as

$$\mathcal{L}_{Z\tilde\nu^I\tilde\nu^R} = \frac{1}{2}\tilde\nu_i^I\Big[\Big(g_1\cos\theta'_W\sin\theta_W + g_2\cos\theta_W\cos\theta'_W - (g_{YB}+g_B)\sin\theta'_W\Big)\sum_{a=1}^{3}Z^{I,*}_{i,a}Z^{R,*}_{j,a} - g_B\sin\theta'_W\sum_{a=1}^{3}Z^{I,*}_{i,3+a}Z^{R,*}_{j,3+a}\Big](p_\mu^{\nu_i^I} - p_\mu^{\nu_j^R})\tilde\nu_j^R Z_\mu. \tag{11}$$

We also deduce the vertex of $Z-\chi_i^0-\chi_j^0$:

$$\begin{aligned} \mathcal{L}_{Z\chi^0\chi^0} = \frac{i}{2}\chi_i^0\Big\{&\Big[(g_{YB}\sin\theta'_W - g_1\cos\theta'_W\sin\theta_W - g_2\cos\theta_W\cos\theta'_W)(N^*_{j3}N_{i3} - N^*_{j4}N_{i4}) + 2g_B\sin\theta'_W(N^*_{j6}N_{i6} - N^*_{j7}N_{i7})\Big]\gamma_\mu P_L \\ &+ \Big[(g_1\cos\theta'_W\sin\theta_W + g_2\cos\theta_W\cos\theta'_W - g_{YB}\sin\theta'_W)(N^*_{i3}N_{j3} - N^*_{i4}N_{j4}) - 2g_B\sin\theta'_W(N^*_{i6}N_{j6} - N^*_{i7}N_{j7})\Big]\gamma_\mu P_R\Big\}\chi_j^0 Z_\mu. \end{aligned} \tag{12}$$

The vertices of $Z-\bar{d}_i-d_j$ and $Z-\bar{u}_i-u_j$ are

$$\mathcal{L}_{Zd\bar{d}}=\frac{\mathrm{i}}{6}\bar{d}_i\Big\{\Big[3g_2\cos\theta_W\cos\theta'_W+g_1\cos\theta'_W\sin\theta_W-(g_{YB}+g_B)\sin\theta'_W\Big]\gamma_\mu P_L+\Big[(2g_{YB}-g_B)\sin\theta'_W-2g_1\cos\theta'_W\sin\theta_W\Big]\gamma_\mu P_R\Big\}d_jZ_\mu, \tag{13}$$

$$\mathcal{L}_{Zu\bar{u}}=\frac{\mathrm{i}}{6}\bar{u}_i\Big\{\Big[g_1\cos\theta'_W\sin\theta_W-3g_2\cos\theta_W\cos\theta'_W-(g_{YB}+g_B)\sin\theta'_W\Big]\gamma_\mu P_L+\Big[4g_1\cos\theta'_W\sin\theta_W-(4g_{YB}+g_B)\sin\theta'_W\Big]\gamma_\mu P_R\Big\}u_jZ_\mu. \tag{14}$$

To save space in the text, the remaining vertices can be found in Ref. [20].

III. ANALYTICAL FORMULA

In this section, we systematically study the amplitudes and branching ratios of the LFV processes $\tau\to e\pi^+\pi^-$, $\tau\to e\pi^+K^-$, and $\tau\to eK^+K^-$ in N-B-LSSM. To ensure a comprehensive analysis, we construct all the relevant Feynman diagrams, including penguin-type, self-energy-type, and box-type diagrams. Then, we give the effective amplitudes of the processes at the quark level.

A. Penguin-type diagrams

When the external leptons are all on shell, and the required Wilson coefficients are extracted, the contribution from the γ-penguin-type diagram in Fig. 1(a) can be written as

$$\begin{aligned}\mathcal{M}^{(a)}_{\gamma-p}=&\frac{-Q_qe^2}{k^2}\sum_{F=\chi^0,\chi^\pm}\sum_{S=\tilde{e},\tilde{\nu}}\{\frac{1}{2}I_1(x_F,x_S)H_R^{SF\bar{e}}H_L^{S^*\tau\bar{F}}\\&+[I_2(x_F,x_S)-I_3(x_F,x_S)]\\&\times[m_F(m_eH_L^{SF\bar{e}}H_L^{S^*\tau\bar{F}}+m_\tau H_R^{SF\bar{e}}H_R^{S^*\tau\bar{F}})]\\&+[I_2(x_F,x_S)-I_4(x_F,x_S)]\\&\times[m_em_\tau H_L^{SF\bar{e}}H_R^{S^*\tau\bar{F}}+(m_\tau^2+m_e^2)H_R^{SF\bar{e}}H_L^{S^*\tau\bar{F}}]\}\\&\times(\bar{e}\gamma^\mu P_L\tau)(\bar{q}\gamma_\mu P_Lq+\bar{q}\gamma_\mu P_Rq)+(L\leftrightarrow R).\end{aligned} \tag{15}$$

In these formulas, $P_L=\frac{1-\gamma_5}{2}$, $P_R=\frac{1+\gamma_5}{2}$, $Q_u=\frac{2}{3}$, and $Q_d=-\frac{1}{3}$. Additionally, $x_i=\frac{m_i^2}{\Lambda^2}$, where m_i denotes the mass of the corresponding particle, Λ represents the energy scale of NP, and k expresses the characteristic energy scale of QCD. $H_{L,R}^{SF\bar{e}}$ and $H_{L,R}^{S^*\tau\bar{F}}$ are the corresponding couplings of the left(right)-hand parts in the Lagrangian. The concrete expressions for form factors I_i (i=1,...,4) are gathered here:

$$\begin{aligned}I_1(x_1,x_2)&=\frac{1}{16\pi^2}\left[\frac{x_1}{x_1-x_2}+\frac{(2x_1-x_2)x_2\ln x_2-x_1^2\ln x_1}{(x_1-x_2)^2}\right],\\I_2(x_1,x_2)&=\frac{1}{96\Lambda^2\pi^2}\left[\frac{11x_1^2-7x_1x_2+2x_2^2}{(x_1-x_2)^3}+\frac{6x_1^3(\ln x_2-\ln x_1)}{(x_1-x_2)^4}\right],\\I_3(x_1,x_2)&=\frac{1}{16\Lambda^2\pi^2}\left[\frac{1}{x_1-x_2}+\frac{x_1(\ln x_2-\ln x_1)}{(x_1-x_2)^2}\right],\\I_4(x_1,x_2)&=\frac{1}{32\Lambda^2\pi^2}\left[\frac{3x_1-x_2}{(x_1-x_2)^2}+\frac{2x_1^2(\ln x_2-\ln x_1)}{(x_1-x_2)^3}\right].\end{aligned} \tag{16}$$

Similarly, the effective amplitude from the γ-penguin-type diagram drawn in Fig. 1(b) is as follows:

$$\begin{aligned}\mathcal{M}^{(b)}_{\gamma-p}=&\frac{Q_qe^2}{k^2}\sum_{F=\chi^0,\chi^\pm}\sum_{S=\tilde{e},\tilde{\nu}}\Big\{\Big[\frac{1}{2}I_1(x_F,x_S)-m_F^2I_3(x_F,x_S)\Big]H_R^{SF\bar{e}}H_L^{S^*\tau\bar{F}}+[I_4(x_F,x_S)-I_3(x_F,x_S)][m_F(m_eH_L^{SF\bar{e}}H_L^{S^*\tau\bar{F}}+m_\tau H_R^{SF\bar{e}}H_R^{S^*\tau\bar{F}})]\\&+[2I_4(x_F,x_S)-I_2(x_F,x_S)-I_3(x_F,x_S)][m_em_\tau H_L^{SF\bar{e}}H_R^{S^*\tau\bar{F}}+(m_\tau^2+m_e^2)H_R^{SF\bar{e}}H_L^{S^*\tau\bar{F}}]\Big\}(\bar{e}\gamma^\mu P_L\tau)(\bar{q}\gamma_\mu P_Lq+\bar{q}\gamma_\mu P_Rq)+(L\leftrightarrow R).\end{aligned} \tag{17}$$

The contributions from Z-penguin-type diagrams are derived in the same way as that done for the γ-penguin-type diagrams:

$$\mathcal{M}^{(a)}_{Z-p} = \sum_{F=\chi^0,\chi^\pm}\sum_{S=\tilde{e},\tilde{\nu}}\Big\{\frac{1}{2m_Z^2}I_5(x_F,x_{S_1},x_{S_2})[H_R^{S_2F\bar{e}}H_L^{S^*\tau\bar{F}}H^{ZS_1S_1^*}H_L^{\bar{q}Zq}\times(\bar{e}\gamma^\mu P_L\tau)(\bar{q}\gamma_\mu P_L q)+H_R^{S_2F\bar{e}}H_L^{S^*\tau\bar{F}}H^{ZS_1S_1^*}H_R^{\bar{q}Zq}$$
$$\times(\bar{e}\gamma^\mu P_L\tau)(\bar{q}\gamma_\mu P_R q)]+(L\leftrightarrow R)\Big\}. \tag{18}$$

$$\mathcal{M}^{(b)}_{Z-p} = \sum_{F=\chi^0,\chi^\pm}\sum_{S=\tilde{e},\tilde{\nu}}\Big\{-\frac{1}{2m_Z^2}I_5(x_S,x_{F_2},x_{F_1})[H_R^{SF_2\bar{e}}H_R^{ZF_1\bar{F}_2}H_L^{S^*\tau\bar{F}_1}H_L^{\bar{q}Zq}\times(\bar{e}\gamma^\mu P_L\tau)(\bar{q}\gamma_\mu P_L q)+H_R^{SF_2\bar{e}}H_R^{ZF_1\bar{F}_2}H_L^{S^*\tau\bar{F}_1}H_R^{\bar{q}Zq}$$
$$\times(\bar{e}\gamma^\mu P_L\tau)(\bar{q}\gamma_\mu P_R q)]+\frac{m_{F_1}m_{F_2}}{m_Z^2}I_6(x_S,x_{F_2},x_{F_1})[H_R^{SF_2\bar{e}}H_L^{ZF_1\bar{F}_2}H_L^{S^*\tau\bar{F}_1}H_L^{\bar{q}Zq}\times(\bar{e}\gamma^\mu P_L\tau)(\bar{q}\gamma_\mu P_L q)$$
$$+H_R^{SF_2\bar{e}}H_L^{ZF_1\bar{F}_2}H_L^{S^*\tau\bar{F}_1}H_R^{\bar{q}Zq}\times(\bar{e}\gamma^\mu P_L\tau)(\bar{q}\gamma_\mu P_R q)]+(L\leftrightarrow R)\Big\}. \tag{19}$$

The functions $I_5(x_1,x_2,x_3)$ and $I_6(x_1,x_2,x_3)$ are

$$I_5(x_1,x_2,x_3)=\frac{1}{16\pi^2}\left[1-\frac{x_1^2\ln x_1}{(x_1-x_2)(x_1-x_3)}+\frac{x_2^2\ln x_2}{(x_1-x_2)(x_2-x_3)}-\frac{x_3^2\ln x_3}{(x_1-x_3)(x_2-x_3)}\right],$$
$$I_6(x_1,x_2,x_3)=\frac{1}{16\Lambda^2\pi^2}\left[\frac{x_1\ln x_1}{(x_1-x_2)(x_1-x_3)}-\frac{x_2\ln x_2}{(x_1-x_2)(x_2-x_3)}+\frac{x_3\ln x_3}{(x_1-x_3)(x_2-x_3)}\right]. \tag{20}$$

After detailed analysis, we conclude that the contribution from the $W-\nu$ diagrams can be reasonably neglected under the current model and energy scale, primarily for the following reason: In N-B-LSSM, the LFV processes of the $W-\nu$ diagrams originate mainly from neutrinos Yukawa couplings Y_ν. In the rotation matrix Z^ν introduced by the diagonalization of the neutrino mass matrix, the magnitude of the off-diagonal element $Z^\nu_{i\neq j}$ can be approximately estimated as $Z^\nu_{i\neq j}=\frac{v_u}{2v_\eta}\cdot\frac{Y_\nu^T}{Y_X}$. Because $Y_\nu^{ij}(i\neq j)$ itself is extremely small (typically $\lesssim 10^{-6}$), and $v_u\ll v_\eta$, the off-diagonal element is usually in the order of 10^{-9} or even smaller. The $W-\nu$ diagram brings in a $Z^\nu_{i\neq j}$ at each vertex, and its overall contribution is $Z^\nu_{ij}Z^\nu_{ji}\sim 10^{-18}$. Based on the above consideration, we prioritize the calculations for other diagrams, particularly those in-

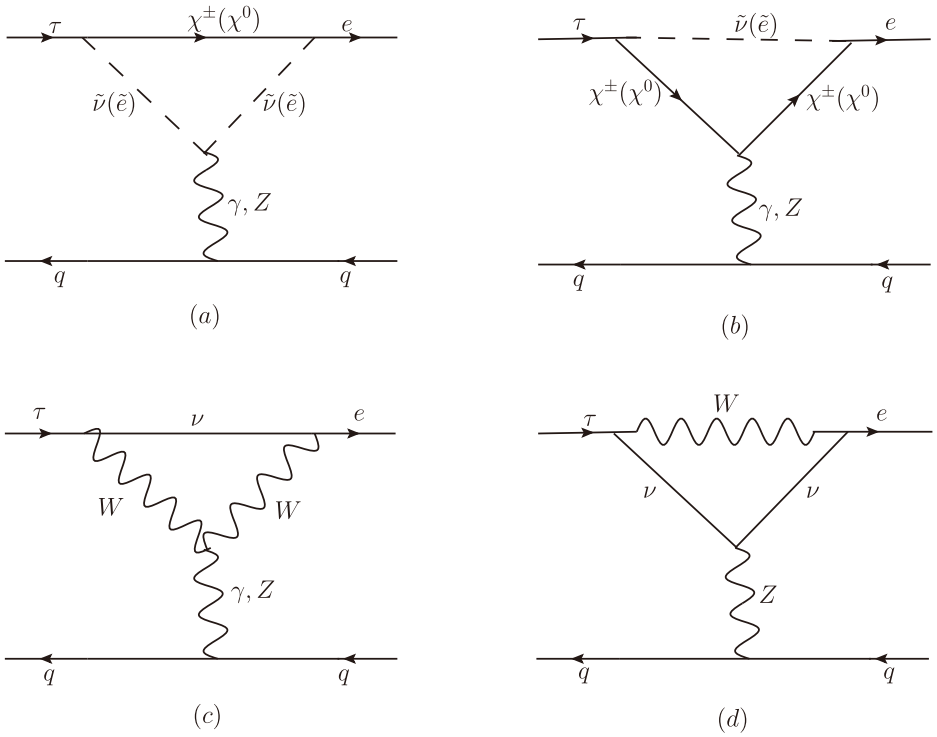

Fig. 1. Penguin-type diagrams for LFV processes $\tau\to e\pi^+\pi^-$, $\tau\to e\pi^+K^-$, and $\tau\to eK^+K^-$ in the N-B-LSSM.

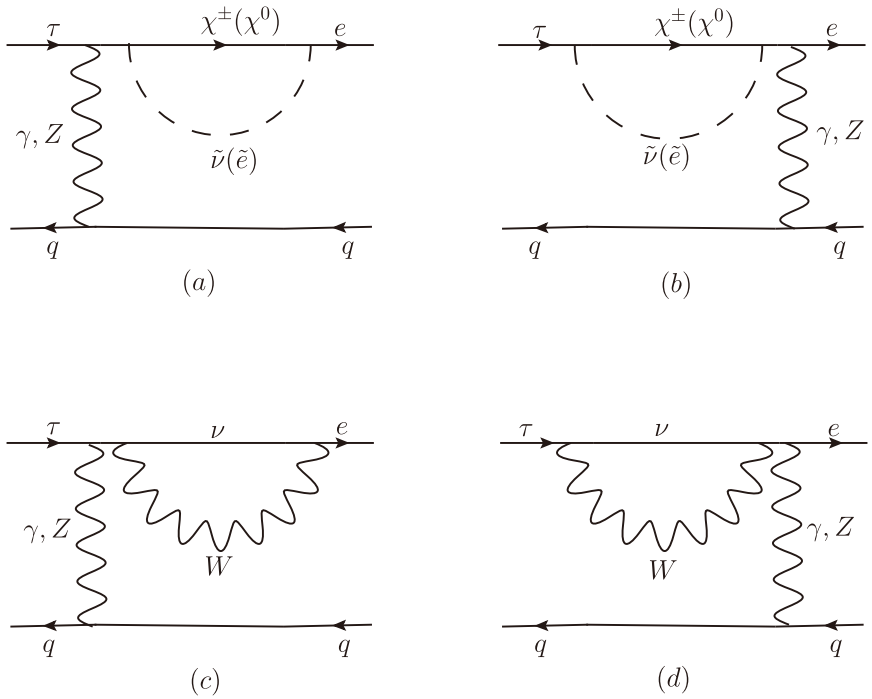

Fig. 2. Self-energy-type diagrams for the LFV processes $\tau \to e\pi^+\pi^-$, $\tau \to e\pi^+K^-$, and $\tau \to eK^+K^-$ in N-B-LSSM.

volving contributions from NP, while omitting further computations for the $W-\nu$ diagrams. Similarly, as with the penguin-type diagrams, the corrections generated by $W-\nu$ for the self-energy-type and box-type diagrams are not presented to save space.

B. Self-energy-type diagrams

We show the specific contribution form of the self-energy-type diagrams in Fig. 2. The γ-self-energy-type diagrams give the following terms:

$$\mathcal{M}^{(a)}_{\gamma-S} = \frac{Q_q e^2}{k^2(m_e^2-m_\tau^2)} \sum_{F=\chi^0,\mathcal{H}^\pm} \sum_{S=\tilde{e},\tilde{\nu}} \Big\{ \frac{1}{2} I_1(x_F,x_S)[m_e(m_e H_R^{S^*F\bar{e}} H_L^{S\tau\bar{F}} + m_\tau H_L^{S^*F\bar{e}} H_R^{S\tau\bar{F}})] + \{m_e^2[I_3(x_F,x_S) - I_4(x_F,x_S)] - I_7(x_F,x_S)\} \times [m_F(m_e H_L^{S^*F\bar{e}} H_L^{S\tau\bar{F}} + m_\tau H_R^{S^*F\bar{e}} H_R^{S\tau\bar{F}})] \Big\} \times (\bar{e}\gamma^\mu P_L \tau)(\bar{q}\gamma_\mu P_L q + \bar{q}\gamma_\mu P_R q) + (L \leftrightarrow R). \tag{21}$$

$$\mathcal{M}^{(b)}_{\gamma-S} = \frac{Q_q e^2}{k^2(m_\tau^2-m_e^2)} \sum_{F=\chi^0,\mathcal{H}^\pm} \sum_{S=\tilde{e},\tilde{\nu}} \Big\{ \frac{1}{2} I_1(x_F,x_S)[m_\tau(m_\tau H_R^{S^*F\bar{e}} H_L^{S\tau\bar{F}} + m_e H_L^{S^*F\bar{e}} H_R^{S\tau\bar{F}})] + \{m_\tau^2[I_3(x_F,x_S) - I_4(x_F,x_S)] - I_7(x_F,x_S)\} \times [m_F(m_e H_L^{S^*F\bar{e}} H_L^{S\tau\bar{F}} + m_\tau H_R^{S^*F\bar{e}} H_R^{S\tau\bar{F}})] \Big\} \times (\bar{e}\gamma^\mu P_L \tau)(\bar{q}\gamma_\mu P_L q + \bar{q}\gamma_\mu P_R q) + (L \leftrightarrow R). \tag{22}$$

For these formulas,

$$I_7(x_1,x_2) = \frac{1}{16\pi^2}\Big[1 + \frac{x_1 \ln x_1}{x_2-x_1} + \frac{x_2 \ln x_2}{x_1-x_2}\Big]. \tag{23}$$

Furthermore, the effective amplitudes from the Z-self-energy-type diagrams drawn in Fig. 2 can be written as

$$\begin{aligned}\mathcal{M}^{(a)}_{Z-S} = {} & \frac{1}{(k^2-m_Z^2)(m_e^2-m_\tau^2)} \sum_{F=\chi^0,\mathcal{H}^\pm} \sum_{S=\tilde{e},\tilde{\nu}} \Big\{ -\frac{1}{2} I_1(x_F,x_S)[m_e(m_e H_R^{S^*F\bar{e}} H_L^{S\tau\bar{F}} H_L^{Z\tau\bar{e}} H_L^{\bar{q}Zq} + m_\tau H_L^{S^*F\bar{e}} H_R^{S\tau\bar{F}} H_L^{Z\tau\bar{e}} H_L^{\bar{q}Zq})] + \{m_e^2[I_4(x_F,x_S) \\ & - I_3(x_F,x_S)] + I_7(x_F,x_S)\} \times [m_F(m_e H_L^{S^*F\bar{e}} H_L^{S\tau\bar{F}} H_L^{Z\tau\bar{e}} H_L^{\bar{q}Zq} + m_\tau H_R^{S^*F\bar{e}} H_R^{S\tau\bar{F}} H_L^{Z\tau\bar{e}} H_L^{\bar{q}Zq})] \Big\} \times (\bar{e}\gamma^\mu P_L \tau)(\bar{q}\gamma_\mu P_L q) \\ & + \Big\{ -\frac{1}{2} I_1(x_F,x_S)[m_e(m_e H_R^{S^*F\bar{e}} H_L^{S\tau\bar{F}} H_L^{Z\tau\bar{e}} H_R^{\bar{q}Zq} + m_\tau H_L^{S^*F\bar{e}} H_R^{S\tau\bar{F}} H_L^{Z\tau\bar{e}} H_R^{\bar{q}Zq})] + \{m_e^2[I_4(x_F,x_S) - I_3(x_F,x_S)] + I_7(x_F,x_S)\} \\ & \times [m_F(m_e H_L^{S^*F\bar{e}} H_L^{S\tau\bar{F}} H_L^{Z\tau\bar{e}} H_R^{\bar{q}Zq} + m_\tau H_R^{S^*F\bar{e}} H_R^{S\tau\bar{F}} H_L^{Z\tau\bar{e}} H_R^{\bar{q}Zq})] \Big\} \times (\bar{e}\gamma^\mu P_L \tau)(\bar{q}\gamma_\mu P_R q) + (L \leftrightarrow R).\end{aligned} \tag{24}$$

$$\mathcal{M}^{(b)}_{Z-S} = \frac{1}{(k^2-m_Z^2)(m_\tau^2-m_e^2)} \sum_{F=\chi^0,\mathcal{X}^\pm} \sum_{S=\tilde{e},\tilde{\nu}} \Big\{ -\frac{1}{2} I_1(x_F,x_S)[m_\tau(m_\tau H_L^{Z\tau\bar{e}} H_R^{S^*F\bar{e}} H_L^{S\tau\bar{F}} H_L^{\bar{q}Zq} + m_e H_L^{Z\tau\bar{e}} H_L^{S^*F\bar{e}} H_R^{S\tau\bar{F}} H_L^{\bar{q}Zq})]$$
$$+ \{m_\tau^2[I_4(x_F,x_S) - I_3(x_F,x_S)] + I_7(x_F,x_S)\} \times [m_F(m_\tau H_L^{Z\tau\bar{e}} H_R^{S^*F\bar{e}} H_R^{S\tau\bar{F}} H_L^{\bar{q}Zq} + m_e H_L^{Z\tau\bar{e}} H_L^{S^*F\bar{e}} H_L^{S\tau\bar{F}} H_L^{\bar{q}Zq})]\Big\}$$
$$\times (\bar{e}\gamma^\mu P_L\tau)(\bar{q}\gamma_\mu P_L q) + \Big\{ -\frac{1}{2} I_1(x_F,x_S)[m_\tau(m_\tau H_L^{Z\tau\bar{e}} H_R^{S^*F\bar{e}} H_L^{S\tau\bar{F}} H_R^{\bar{q}Zq} + m_e H_L^{Z\tau\bar{e}} H_L^{S^*F\bar{e}} H_R^{S\tau\bar{F}} H_R^{\bar{q}Zq})]$$
$$+ \{m_\tau^2[I_4(x_F,x_S) - I_3(x_F,x_S)] + I_7(x_F,x_S)\} \times [m_F(m_\tau H_L^{Z\tau\bar{e}} H_R^{S^*F\bar{e}} H_R^{S\tau\bar{F}} H_R^{\bar{q}Zq} + m_e H_L^{Z\tau\bar{e}} H_L^{S^*F\bar{e}} H_L^{S\tau\bar{F}} H_R^{\bar{q}Zq})]\Big\}$$
$$\times (\bar{e}\gamma^\mu P_L\tau)(\bar{q}\gamma_\mu P_R q) + (L \leftrightarrow R). \tag{25}$$

C. Box-type diagrams

The box-type diagrams contributing to the LFV processes $\tau \to e\pi^+\pi^-$, $\tau \to e\pi^+K^-$, and $\tau \to eK^+K^-$ in the N-B-LSSM are shown in Fig. 3. Fierz rearrangement is carried out in the calculation processes. Fig. 3(a)(b) represent the contributions from neutral fermions χ^0, charged scalars $\tilde{e}$, and squark $\tilde{q}$ ($\tilde{q}$=$\tilde{u}$, $\tilde{d}$). We analyze the effective amplitudes $\mathcal{M}^{(a)}_{(n)}$ and $\mathcal{M}^{(b)}_{(n)}$ originating from those box diagrams with virtual neutral fermion contributions in a concrete form:

$$\mathcal{M}^{(a)}_{(n)} = \sum_{F_1,F_2=\chi^0,\mathcal{X}^0} \sum_{S_1,S_2=\tilde{e},\tilde{q}} \Big\{ \frac{1}{2} I_8(x_{F_1},x_{F_2},x_{S_1},x_{S_2}) \Big[\frac{1}{2} H_L^{S_1^*\tau\bar{F}_1} H_R^{S_1F_2\bar{e}} H_R^{S_2F_1\bar{q}} H_L^{S_2^*qF_2} \times (\bar{e}\gamma^\mu P_L\tau)(\bar{q}\gamma_\mu P_L q)$$
$$- H_R^{S_1^*\tau\bar{F}_1} H_R^{S_1F_2\bar{e}} H_L^{S_2F_1\bar{q}} H_L^{S_2^*qF_2} \times (\bar{e}P_R\tau)(\bar{q}P_L q)\Big] + \frac{1}{8} I_9(x_{F_1},x_{F_2},x_{S_1},x_{S_2}) \Big[m_{F_1} m_{F_2} H_L^{S_1^*\tau\bar{F}_1} H_L^{S_1F_2\bar{e}} H_L^{S_2F_1\bar{q}} H_L^{S_2^*qF_2}$$
$$\times [(\bar{e}P_R\tau)(\bar{q}P_R q) - (\bar{e}P_R\tau)(\bar{q}P_L q) - (\bar{e}P_L\tau)(\bar{q}P_R q) - 3(\bar{e}P_L\tau)(\bar{q}P_L q) - (\bar{e}\sigma_{\mu\nu}P_L\tau)(\bar{q}\sigma^{\mu\nu}P_L q) - (\bar{e}\sigma_{\mu\nu}P_R\tau)(\bar{q}\sigma^{\mu\nu}P_L q)]$$
$$+ H_R^{S_1^*\tau\bar{F}_1} H_L^{S_1F_2\bar{e}} H_R^{S_2F_1\bar{q}} H_L^{S_2^*qF_2} \times [-4(\bar{e}\gamma^\mu P_R\tau)(\bar{q}\gamma_\mu P_L q) + (\bar{e}P_R\tau)(\bar{q}P_R q) - (\bar{e}P_R\tau)(\bar{q}P_L q)$$
$$- (\bar{e}P_L\tau)(\bar{q}P_R q) + (\bar{e}P_L\tau)(\bar{q}P_L q)]\Big] + (L \leftrightarrow R)\Big\}. \tag{26}$$

$$\mathcal{M}^{(b)}_{(n)} = \sum_{F_1,F_2=\chi^0,\mathcal{X}^0} \sum_{S_1,S_2=\tilde{e},\tilde{q}} \Big\{ \frac{1}{2} I_8(x_{F_1},x_{F_2},x_{S_1},x_{S_2}) \Big[\frac{1}{2} H_L^{S_1^*\tau\bar{F}_1} H_R^{S_1F_2\bar{e}} H_L^{S_2F_2\bar{q}} H_R^{S_2^*qF_1} \times (\bar{e}\gamma^\mu P_L\tau)(\bar{q}\gamma_\mu P_R q)$$
$$+ H_L^{S_1^*\tau\bar{F}_1} H_L^{S_1F_2\bar{e}} H_R^{S_2F_2\bar{q}} H_R^{S_2^*qF_1} \times (\bar{e}P_L\tau)(\bar{q}P_R q)\Big] + I_9(x_{F_1},x_{F_2},x_{S_1},x_{S_2}) \Big[\frac{m_{F_1} m_{F_2}}{2} H_L^{S_1^*\tau\bar{F}_1} H_L^{S_1F_2\bar{e}} H_L^{S_2F_2\bar{q}} H_L^{S_2^*qF_1} (\bar{e}P_L\tau)(\bar{q}P_L q)$$

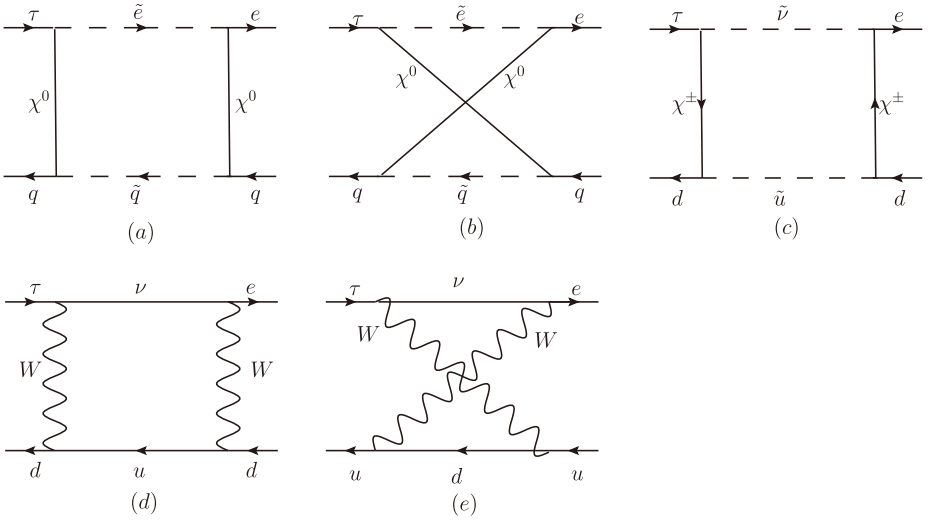

Fig. 3. Box-type diagrams for the LFV processes $\tau \to e\pi^+\pi^-$, $\tau \to e\pi^+K^-$, and $\tau \to eK^+K^-$ in N-B-LSSM.

$$+\frac{1}{8}H_L^{S_1^*\tau\bar{F}_1}H_L^{S_1F_2\bar{e}}H_L^{S_2F_2\bar{q}}H_L^{S_2^*q\bar{F}_1}[(\bar{e}P_L\tau)(\bar{q}P_Rq)+(\bar{e}P_R\tau)(\bar{q}P_Lq)-(\bar{e}P_R\tau)(\bar{q}P_Rq)-(\bar{e}P_L\tau)(\bar{q}P_Lq)$$
$$-(\bar{e}\sigma_{\mu\nu}P_R\tau)(\bar{q}\sigma^{\mu\nu}P_Lq)-(\bar{e}\sigma_{\mu\nu}P_L\tau)(\bar{q}\sigma^{\mu\nu}P_Lq)]+\frac{1}{8}H_R^{S_1^*\tau\bar{F}_1}H_L^{S_1F_2\bar{e}}H_L^{S_2F_2\bar{q}}H_R^{S_2^*q\bar{F}_1}[(\bar{e}P_R\tau)(\bar{q}P_Lq)$$
$$+(\bar{e}P_L\tau)(\bar{q}P_Rq)-(\bar{e}P_L\tau)(\bar{q}P_Lq)-(\bar{e}P_R\tau)(\bar{q}P_Rq)-4(\bar{e}\gamma^\mu P_R\tau)(\bar{q}\gamma_\mu P_Rq)]\Big]+(L\leftrightarrow R)\Big\}. \tag{27}$$

The concrete expressions for the functions $I_8(x_1,x_2,x_3,x_4)$ and $I_9(x_1,x_2,x_3,x_4)$ are defined as follows:

$$I_8(x_1,x_2,x_3,x_4)=\frac{1}{16\Lambda^2\pi^2}\Big[\frac{x_1^2\ln x_1}{(x_1-x_2)(x_1-x_3)(x_1-x_4)}-\frac{x_2^2\ln x_2}{(x_1-x_2)(x_2-x_3)(x_2-x_4)}+\frac{x_3^2\ln x_3}{(x_1-x_3)(x_2-x_3)(x_3-x_4)}$$
$$-\frac{x_4^2\ln x_4}{(x_1-x_4)(x_2-x_4)(x_3-x_4)}\Big].$$
$$I_9(x_1,x_2,x_3,x_4)=\frac{1}{16\Lambda^4\pi^2}\Big[-\frac{x_1\ln x_1}{(x_1-x_2)(x_1-x_3)(x_1-x_4)}+\frac{x_2\ln x_2}{(x_1-x_2)(x_2-x_3)(x_2-x_4)}-\frac{x_3\ln x_3}{(x_1-x_3)(x_2-x_3)(x_3-x_4)}$$
$$+\frac{x_4\ln x_4}{(x_1-x_4)(x_2-x_4)(x_3-x_4)}\Big]. \tag{28}$$

Correspondingly, Fig. 3(c) represents the contribution from charged fermions $\chi^\pm$, neutral scalars $\tilde{\nu}$, and squark $\tilde{u}$. The effective amplitude $\mathcal{M}_{(c)}$ from the box diagram with virtual charged fermion contribution is

$$\mathcal{M}_{(c)}=\sum_{F_1,F_2=\chi^\pm,\chi^\pm}\sum_{S_1,S_2=\tilde{\nu},\tilde{u}}\Big\{\frac{1}{2}I_8(x_{F_1},x_{F_2},x_{S_1},x_{S_2})\Big[\frac{1}{2}H_L^{S_1\tau\bar{F}_1}H_R^{S_1F_2\bar{e}}H_R^{S_2F_1\bar{d}}H_L^{S_2d\bar{F}_2}\times(\bar{e}\gamma^\mu P_L\tau)(\bar{d}\gamma_\mu P_Ld)$$
$$-H_R^{S_1\tau\bar{F}_1}H_R^{S_1F_2\bar{e}}H_L^{S_2F_1\bar{d}}H_L^{S_2d\bar{F}_2}\times(\bar{e}P_R\tau)(\bar{d}P_Ld)\Big]+\frac{1}{8}I_9(x_{F_1},x_{F_2},x_{S_1},x_{S_2})\Big[m_{F_1}m_{F_2}H_L^{S_1\tau\bar{F}_1}H_L^{S_1F_2\bar{e}}H_L^{S_2F_1\bar{d}}H_L^{S_2d\bar{F}_2}$$
$$\times[(\bar{e}P_R\tau)(\bar{d}P_Rd)-(\bar{e}P_R\tau)(\bar{d}P_Ld)-(\bar{e}P_L\tau)(\bar{d}P_Rd)-3(\bar{e}P_L\tau)(\bar{d}P_Ld)-(\bar{e}\sigma_{\mu\nu}P_L\tau)(\bar{d}\sigma^{\mu\nu}P_Ld)-(\bar{e}\sigma_{\mu\nu}P_R\tau)(\bar{d}\sigma^{\mu\nu}P_Ld)]$$
$$+H_R^{S_1\tau\bar{F}_1}H_L^{S_1F_2\bar{e}}H_R^{S_2F_1\bar{d}}H_L^{S_2d\bar{F}_2}\times[-4(\bar{e}\gamma^\mu P_R\tau)(\bar{d}\gamma_\mu P_Ld)+(\bar{e}P_R\tau)(\bar{d}P_Rd)-(\bar{e}P_R\tau)(\bar{d}P_Ld)$$
$$-(\bar{e}P_L\tau)(\bar{d}P_Rd)+(\bar{e}P_L\tau)(\bar{d}P_Ld)]\Big]+(L\leftrightarrow R)\Big\}. \tag{29}$$

D. Using MIA to calculate $\tau \to eM^+M^-$

In this work, we primarily adopt the mass eigenstate method for our calculations. This method allows for a systematic and precise treatment of particle mixing, mass spectra, and complete one-loop contributions. It enables us to include all physical states and their interactions comprehensively, thus ensuring the rigor and accuracy of our results. However, because of the involvement of multiple mixing matrices, rotation matrices, and mass eigenvalues, the resulting expressions are often complex, making it less straightforward to identify which parameters play the dominant role in the LFV processes. This complexity can obscure physical intuition, especially regarding the sensitivity of specific parameters.

Representative mass insertion diagrams for the process $\tau \to eM^+M^-$ in N-B-LSSM are presented in Fig. 4. The advantage of the mass insertion approximation (MIA) method lies in its ability to express flavor violation explicitly through mass insertions $\Delta_{ij}^{AB}(A,B=L,R)$ in the propagators. This enables us to write the LFV amplitudes directly in terms of the off-diagonal components of the soft SUSY breaking slepton mass matrices $m_{\tilde{L}}^2$, $m_{\tilde{E}}^2$ and the trilinear coupling matrix T_e, T_ν. With proper expansions, this approach leads to much simpler analytical expressions, allowing us to clearly identify the dominant contributions to LFV at the analytical level.

As an example, Fig. 4(a) shows a typical one-loop contribution mediated by $\tilde{B}$ and the slepton mass insertions between $\tilde{L}_j^L$ and $\tilde{L}_i^R$, with the amplitude given by

$$\mathcal{M}(\tilde{L}_j^L,\tilde{L}_i^R,\tilde{B})=\frac{-Q_qe^2}{k^2}\frac{M_1(m_e+m_\tau)}{\Lambda^2}\Delta_{ij}^{LR}g_1^2\mathcal{I}(x_1,x_{L_j^L},x_{L_i^R})$$
$$\times(\bar{e}\gamma^\mu P_L\tau)(\bar{q}\gamma_\mu P_Lq+\bar{q}\gamma_\mu P_Rq), \tag{30}$$

where the loop function $\mathcal{I}(x,y,z)$ is given by

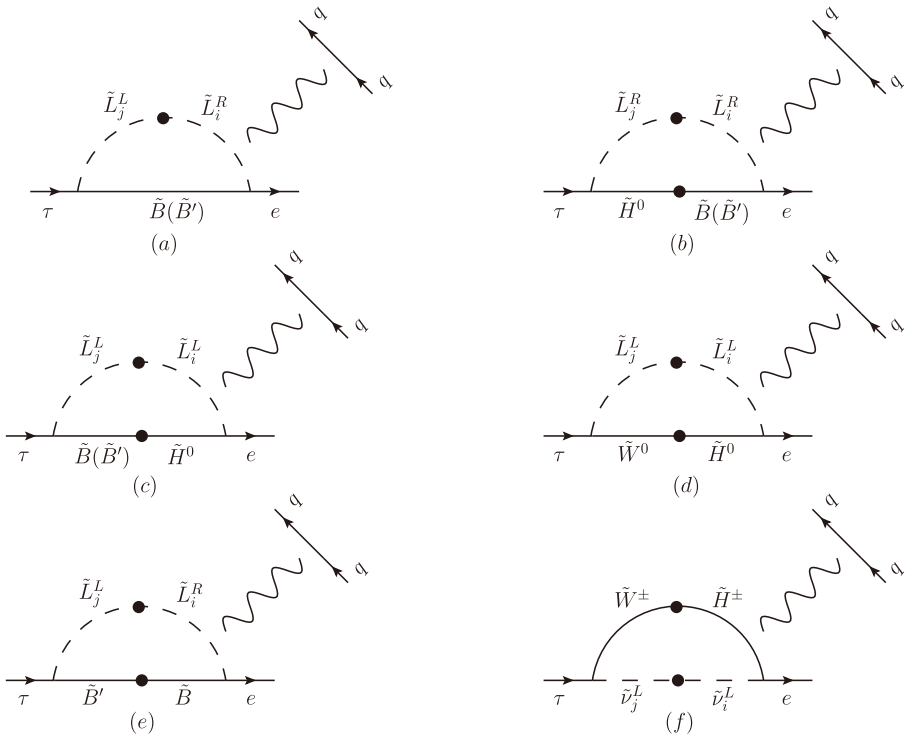

Fig. 4. Feynman diagrams for $\tau \to eM^+M^-$ in MIA.

$$\mathcal{I}(x,y,z) = \frac{1}{16\pi^2}\left[\frac{x\left(x^3-3xyz+yz(y+z)\right)\ln x}{(x-y)^3(x-z)^3} + \frac{-3x^2+x(y+z)+yz}{2(x-y)^2(x-z)^2} - \frac{xy\ln y}{(x-y)^3(y-z)} - \frac{xz\ln z}{(x-z)^3(z-y)}\right]. \tag{31}$$

To better illustrate the parameter dependence, we consider a simplified scenario where all superpartner masses are nearly degenerate:

$$M_1 = m_{\tilde{L}_L} = m_{\tilde{L}_R} = M_{\rm SUSY}. \tag{32}$$

In this degenerate limit, the loop function reduces to a constant $\mathcal{I}(1,1,1) = \dfrac{1}{192\pi^2}$, and the mass insertion can be expressed as

$$\Delta_{ij}^{LR} = m_{l_j} m_{\tilde{L}_L} \delta_{ij}^{LR}. \tag{33}$$

This clearly shows that the LFV amplitude is directly controlled by Δ_{ij}^{LR} including $T_{e_{ij}}$. In a similar way, the other MIA diagrams can also be analyzed, and thus, we do not study them in detail anymore in this work. Overall, the results depend on the off-diagonal elements of $m^2_{\tilde{L},\tilde{E}}$, T_e, and T_ν. Therefore, the simplified expressions clearly reveal the parametric dependence of the LFV amplitudes.

In summary, while the main body of this work is based on the mass eigenstate method to ensure precision and completeness, the inclusion of the MIA method provides an intuitive and analytical perspective on the dependence of the LFV processes on key parameters. This supplementary analysis enhances the physical interpretability of the results and offers a useful framework for exploring other LFV processes in future studies.

E. Branching ratios

Once the effective amplitudes at the quark level are determined, we can calculate the corresponding branching ratios [28]:

$$\begin{aligned}\mathrm{BR}(\tau \to e\pi^+\pi^-) \simeq\ & 1.9\times10^2|\Gamma^e_\gamma|^2_{\tau e} + 1.0\times10^{-8}|C_{GG}|^2 \\ & + 0.13|C^{ed}_{SRR} + C^{ed}_{SRL}|^2_{ss} \\ & + \Big(0.17\Big|[C^{eq}_{SRR} + C^{eq}_{SRL}]_{\tau e(qq)^{(0)}}\Big|^2 \\ & + 0.5\Big|[C^{eq}_{VLL} + C^{eq}_{VLR}]_{\tau e(qq)^{(1)}}\Big|^2\Big) \\ & + 1.0\Big|[C^{ed}_{TRR}]_{\tau edd} - [C^{eu}_{TRR}]_{\tau euu}\Big|^2. \end{aligned} \tag{34}$$

For this formula,

$$(\Gamma^e_\gamma)_{\tau e} = \frac{vem_\tau}{2\sqrt{\alpha\pi}}A_2^R - \frac{16}{3}\Big(\frac{\mathrm{i}\prod_{VT}(0)}{v}\Big)[C^{eu}_{TRR}]_{e\tau uu},$$

$$[C_{GG}]_{\tau e} = \frac{1}{3}\sum_{q=b,c}\frac{v}{m_q}[C^{eq}_{SRR}+C^{eq}_{SRL}]_{\tau eqq},$$
$$(v=\sqrt{v_u^2+v_d^2},\ \alpha\approx\frac{e^2}{\hbar c}). \tag{35}$$

Herein, the non-perturbative parameter $(\mathrm{i}\prod_{VT}(0)/v)\approx 1.6\times10^{-4}$ and the notation $(qq)^{(0),(1)}$ indicate that the isoscalar or isovector $(uu\pm dd)$ combination of Wilson coefficients has to be taken. Meanwhile, A_2^R can be found in Ref.[20].

$$\begin{aligned}\mathrm{BR}(\tau\to e\pi^+K^-) \simeq{}& 0.17\left|C^{ed}_{VLL}+C^{ed}_{VLR}\right|^2_{\tau eds}\\ &+0.16\left|C^{ed}_{SRR}+C^{ed}_{SRL}\right|^2_{\tau eds}.\end{aligned} \tag{36}$$

$$\begin{aligned}\mathrm{BR}(\tau\to eK^+K^-) = {}& 0.59\left|\left(C^{ed}_{VLL}+C^{ed}_{VLR}\right)_{\tau ess}\right|^2\\ &+(1.0\pm0.1)\cdot10^{-2}\left|\left(C^{eu}_{VLL}+C^{eu}_{VLR}\right)_{\tau euu}\right|^2\\ &+(0.6\pm0.2)\cdot10^{-3}\left|\left(C^{ed}_{VLL}+C^{ed}_{VLR}\right)_{\tau edd}\right|^2\\ &-(4.6\pm0.2)\cdot10^{-2}\left(C^{ed}_{VLL}+C^{ed}_{VLR}\right)_{\tau ess}\left(C^{eu}_{VLL}+C^{eu}_{VLR}\right)_{\tau euu}\\ &-(4.3\pm1.5)\cdot10^{-3}\left(C^{ed}_{VLL}+C^{ed}_{VLR}\right)_{\tau ess}\left(C^{ed}_{VLL}+C^{ed}_{VLR}\right)_{\tau edd}\\ &+(3.5\pm0.8)\cdot10^{-3}\left(C^{ed}_{VLL}+C^{ed}_{VLR}\right)_{\tau edd}\left(C^{eu}_{VLL}+C^{eu}_{VLR}\right)_{\tau euu}.\end{aligned} \tag{37}$$

The final Wilson coefficients C^{eq}_{VLL}, C^{eq}_{VLR}, C^{eq}_{SRR}, C^{eq}_{SRL}, and C^{eq}_{TRR} are obtained from the sum of these diagrams' amplitudes. The corresponding effective operators are $(\bar e\gamma^\mu P_L\tau)(\bar q\gamma_\mu P_L q)$, $(\bar e\gamma^\mu P_L\tau)(\bar q\gamma_\mu P_R q)$, $(\bar e P_R\tau)(\bar q P_R q)$, $(\bar e P_R\tau)(\bar q P_L q)$, $(\bar e\sigma^{\mu\nu}P_R\tau)(\bar q\sigma_{\mu\nu}P_R q)$, respectively. For convenience, the final Wilson coefficients are analyzed in the generic form, which can simplify the work. Herein, C^{eq}_{VLL} is used as an example; see Appendix A for the rest.

$$\begin{aligned}C^{eq}_{VLL} = {}& \sum_{F_1,F_2=\chi^\pm,\chi^\pm}\sum_{S_1,S_2=\tilde\nu,\tilde u}\frac{1}{4}I_8(x_{F_1},x_{F_2},x_{S_1},x_{S_2})H_L^{S_1\tau\bar F_1}H_R^{S_1F_2\bar e}H_R^{S_2F_1\bar d}H_L^{S_2d\bar F_2}-\sum_{F_1,F_2=\chi^0,\chi^0}\sum_{S_1,S_2=\tilde e,\tilde q}\\
&\times\frac{1}{2}\Big[I_9(x_{F_1},x_{F_2},x_{S_1},x_{S_2})H_L^{S_1^*\tau\bar F_1}H_R^{S_1F_2\bar e}H_R^{S_2F_2\bar q}H_L^{S_2^*q\bar F_1}-\frac{1}{2}I_8(x_{F_1},x_{F_2},x_{S_1},x_{S_2})H_L^{S_1^*\tau\bar F_1}H_R^{S_1F_2\bar e}H_R^{S_2F_1\bar q}H_L^{S_2^*q\bar F_2}\Big]\\
&+\sum_{F=\chi^0,\chi^\pm}\sum_{S=\tilde e,\tilde\nu}\frac{1}{m_Z^2}\Big[\frac{1}{2}I_5(x_F,x_{S_1},x_{S_2})[H_R^{S_2F\bar e}H_L^{S^*\tau\bar F}H^{ZS_1S_1^*}H_L^{\bar qZq}-H_R^{S_2F\bar e}H_R^{ZF_1\bar F_2}H_L^{S^*\tau\bar F_1}H_L^{\bar qZq}]\\
&+m_{F_1}m_{F_2}I_6(x_S,x_{F_2},x_{F_1})H_R^{S_2F\bar e}H_L^{ZF_1\bar F_2}H_L^{S^*\tau\bar F_1}H_L^{\bar qZq}\Big]+\frac{1}{(m_e^2-m_\tau^2)}\Big[\frac{1}{2}I_1(x_F,x_S)(m_e^2-m_\tau^2)[\frac{Q_qe^2}{k^2}H_R^{S^*F\bar e}H_L^{S\tau\bar F}\\
&-\frac{1}{(k^2-m_Z^2)}H_R^{S^*F\bar e}H_L^{S\tau\bar F}H_L^{Z\tau\bar e}H_L^{\bar qZq}]+(m_e^2-m_\tau^2)[I_3(x_F,x_S)-I_4(x_F,x_S)]\\
&\times[\frac{Q_qe^2}{k^2}m_F(m_eH_L^{S^*F\bar e}H_L^{S\tau\bar F}+m_\tau H_R^{S^*F\bar e}H_R^{S\tau\bar F})-\frac{1}{(k^2-m_Z^2)}\times m_F(m_eH_L^{S^*F\bar e}H_L^{S\tau\bar F}H_L^{Z\tau\bar e}H_L^{\bar qZq}\\
&+m_\tau H_R^{S^*F\bar e}H_R^{S\tau\bar F}H_L^{Z\tau\bar e}H_L^{\bar qZq})]\Big]+\sum_{F=\chi^0}\sum_{S=\tilde e}\frac{-Q_qe^2}{k^2}\Big[\frac{1}{2}I_1(x_F,x_S)H_R^{SF\bar e}H_L^{S^*\tau\bar F}+[I_2(x_F,x_S)-I_4(x_F,x_S)]\\
&\times[(m_\tau^2+m_e^2)H_R^{SF\bar e}H_L^{S^*\tau\bar F}+m_em_\tau H_L^{SF\bar e}H_R^{S^*\tau\bar F}]+[I_2(x_F,x_S)-I_3(x_F,x_S)][m_F(m_eH_L^{SF\bar e}H_L^{S^*\tau\bar F}+m_\tau H_R^{SF\bar e}H_R^{S^*\tau\bar F})]\Big]\\
&+\sum_{F=\chi^\pm}\sum_{S=\tilde\nu}\frac{Q_qe^2}{k^2}\Big[[\frac{1}{2}I_1(x_F,x_S)-m_F^2I_3(x_F,x_S)]H_R^{SF\bar e}H_L^{S^*\tau\bar F}+[2I_4(x_F,x_S)-I_2(x_F,x_S)\\
&-I_3(x_F,x_S)][(m_\tau^2+m_e^2)H_R^{SF\bar e}H_L^{S^*\tau\bar F}+m_em_\tau H_L^{SF\bar e}H_R^{S^*\tau\bar F}]+[I_4(x_F,x_S)-I_3(x_F,x_S)][m_F(m_eH_L^{SF\bar e}H_L^{S^*\tau\bar F}+m_\tau H_R^{SF\bar e}H_R^{S^*\tau\bar F})]\Big].\end{aligned} \tag{38}$$

IV. NUMERICAL RESULTS

In this section, we perform a numerical analysis of LFV processes and systematically investigate the model parameters under current experimental constraints. To obtain reasonable numerical results, several sensitive parameters are explored, and the processes $\tau\to e\pi^+\pi^-$, $\tau\to e\pi^+K^-$, and $\tau\to eK^+K^-$ are discussed in detail in three subsections. Notably, because the experimental upper limit on the $\tau\to e\gamma$ process imposes the most stringent constraints on the parameter space of N-B-LSSM, its impact on LFV must be thoroughly taken into account

[20]. Furthermore, we adopt the lightest CP-even Higgs mass $m_{h^0} = 125.20 \pm 0.11$ GeV [21]. For the mass of the added heavy vector boson Z', the latest experimental constraint is $M_{Z'} > 5.1$ TeV, a significantly stronger bound than previous limits [29]. Given that $M_{Z'}$ is much larger than M_Z, its contribution to the amplitude is negligible and thus not calculated in this work. The lower limit on the ratio $M_{Z'}/g_B$ is set to 6 TeV at 99% C.L. [30, 31]. Considering constraints from LHC data [32−39], we set the following parameter conditions: the slepton mass is greater than 700 GeV, the chargino mass is greater than 1100 GeV, and the squark mass is greater than 1600 GeV, with the experimental value of $\tan\beta_\eta$ being less than 1.5. In addition, the constraints of Charge and Color Breaking (CCB) are also taken into account [40, 41]. Based on these rigorous experimental requirements, we collect extensive data, and the relationships among various parameters are graphically illustrated. Through a systematic analysis of these plots and the experimental upper limits on the branching ratios, we identify a viable parameter space that explains the LFV phenomena.

Considering the above constraints in the front paragraph, we use the following parameters in N-B-LSSM:

$$\begin{aligned}&\tan\beta_\eta = 0.9,\ Y_{Xii} = 0.5,\ T_\lambda = 1\ \text{TeV},\ T_{\lambda_2} = 1\ \text{TeV},\\&T_\kappa = -2.5\ \text{TeV},\ T_{uii} = 1\ \text{TeV},\ T_{dii} = 1\ \text{TeV},\ T_{Xii} = -4\ \text{TeV},\\&M_1 = 0.4\ \text{TeV},\ M_2 = 1.2\ \text{TeV},\ M^2_{\tilde{\nu}ii} = 2.5\ \text{TeV}^2,\ M^2_{\tilde{Q}ii} = 3.1\\&\text{TeV}^2,\ M^2_{\tilde{U}ii} = 2.2\ \text{TeV}^2,\ M^2_{\tilde{D}ii} = 2.8\ \text{TeV}^2,\ (i = 1,2,3).\end{aligned} \tag{39}$$

To simplify the numerical discussion, we employ the parameter relationships and analyze their variations in numerical analysis:

$$\begin{aligned}&\tan\beta,\ g_B,\ g_{YB},\ \lambda,\ \lambda_2,\ v_S,\ \kappa,\ M_{BL},\ M_{BB'},\\&M^2_{\tilde{L}ii} = M^2_{\tilde{L}},\ M^2_{\tilde{E}ii} = M^2_{\tilde{E}},\ M^2_{\tilde{L}ij} = M^2_{\tilde{L}ji},\ M^2_{\tilde{E}ij} = M^2_{\tilde{E}ji},\\&T_{eii} = T_e,\ T_{\nu ii} = T_\nu,\ T_{eij} = T_{eji},\ T_{\nu ij} = T_{\nu ji},\\&(i,j = 1,2,3,\ i \neq j).\end{aligned} \tag{40}$$

Unless declared otherwise, the off-diagonal elements of the used parameters are assumed to be zero.

In the framework of N-B-LSSM, LFV originates primarily from the flavor off-diagonal structures introduced by soft SUSY breaking terms, which violate lepton flavor conservation. At the loop diagram level, these off-diagonal parameters alter the mass eigenstates and interaction vertices of internal SUSY particles, thereby inducing $\tau \to e$ transitions at the effective vertex. The relevant parameters include: (i) the off-diagonal element $M^2_{\tilde{L}13}$ in the left-handed slepton mass matrix, also appearing in the CP-even and CP-odd sneutrino sectors, which induces flavor mixing between $\tilde{e}_L$ and $\tilde{\tau}_L$, significantly contributing to both $\tilde{e}-\chi^0$ and $\tilde{\nu}^{R,I}-\chi^\pm$ loop diagrams; (ii) the off-diagonal element $M^2_{\tilde{E}13}$ in the right-handed slepton mass matrix, responsible for the mixing between $\tilde{e}_R$ and $\tilde{\tau}_R$, which mainly affects the flavor structure of $\tilde{e}-\chi^0$ loop diagrams; (iii) the off-diagonal term $M^2_{\tilde{\nu}13}$ in the sneutrino mass matrix, which influences the masses and mixings of CP-even and CP-odd sneutrinos, and plays a crucial role in $\tilde{\nu}^{R,I}-\chi^\pm$ loop diagrams; (iv) the trilinear coupling T_{e13}, which enhances the couplings between different slepton flavors such as $\tilde{e}_L$ and $\tilde{\tau}_R$, contributing to $\tilde{e}-\chi^0$ loop diagrams; and (v) the sneutrino trilinear coupling $T_{\nu 13}$, which affects the mass spectra and mixings of CP-even and CP-odd sneutrinos, significantly contributes to $\tilde{\nu}^{R,I}-\chi^\pm$ loop diagrams, and is a key parameter determining the LFV transition rates. The effective couplings in the loop diagrams are governed directly by the aforementioned flavor-violating parameters. As such, these parameters collectively determine both the LFV transition mechanisms and the resulting branching ratios. In fact, in addition to the soft-breaking parameters, given the non-zero masses of neutrinos, the CKM-like matrix in the lepton sector is another source of the flavor violation. This source, however, is not important for the processes because of the small mass splitting of neutrinos (like the GIM mechanism).

A. Process of $\tau \to e\pi^+\pi^-$

In the case of parameters $\lambda_2 = -0.25$, $\kappa = 0.1$, $T_\nu = 1$ TeV, $T_e = 1.5$ TeV, $M^2_{\tilde{E}} = 1.7\ \text{TeV}^2$, we draw BR $(\tau \to e\pi^+\pi^-)$ diagrams under the influence of different parameters, as shown in Fig. 5.

Using the parameters $\lambda = 0.4$, $\tan\beta = 25$, $M_{BB'} = 0.1$ TeV, $M_{BL} = 1$ TeV, $v_S = 4$ TeV, $M^2_{\tilde{L}13} = 0.05\ \text{TeV}^2$, $M^2_{\tilde{L}} = 0.16\ \text{TeV}^2$, we plot BR $(\tau \to e\pi^+\pi^-)$ versus g_{YB} in Fig. 5(a), where the blue, green, and purple curves correspond to $g_B = 0.2$, 0.3, 0.4, respectively. It can be clearly seen that for any given g_B, the branching ratio decreases monotonically with increases in g_{YB}; meanwhile, under the same g_{YB} condition, the larger the g_B, the smaller the branching ratio. Specifically, the top curve has successively exceeded the experimental upper limits of $\tau \to e\gamma$ and $\tau \to e\pi^+\pi^-$ in the region of $-0.3 < g_{YB} < -0.22$. The middle curve exceeds the limit of $\tau \to e\gamma$ only in the region of $-0.3 < g_{YB} < -0.24$, while the bottom curve remains below the existing experimental constraints throughout the entire scanned range. g_B is the $U(1)_{B-L}$ gauge coupling constant. The mass matrices of several particles (neutralino, slepton, CP-even sneutrino, CP-odd sneutrino, up-squark, down-squark, CP-even Higgs) all have the important parameter g_B, which can improve the NP effect. g_{YB} is the coupling constant for gauge mixing of $U(1)_Y$ and $U(1)_{B-L}$, which is a new parameter beyond MSSM and can bring new effect. The formation of this

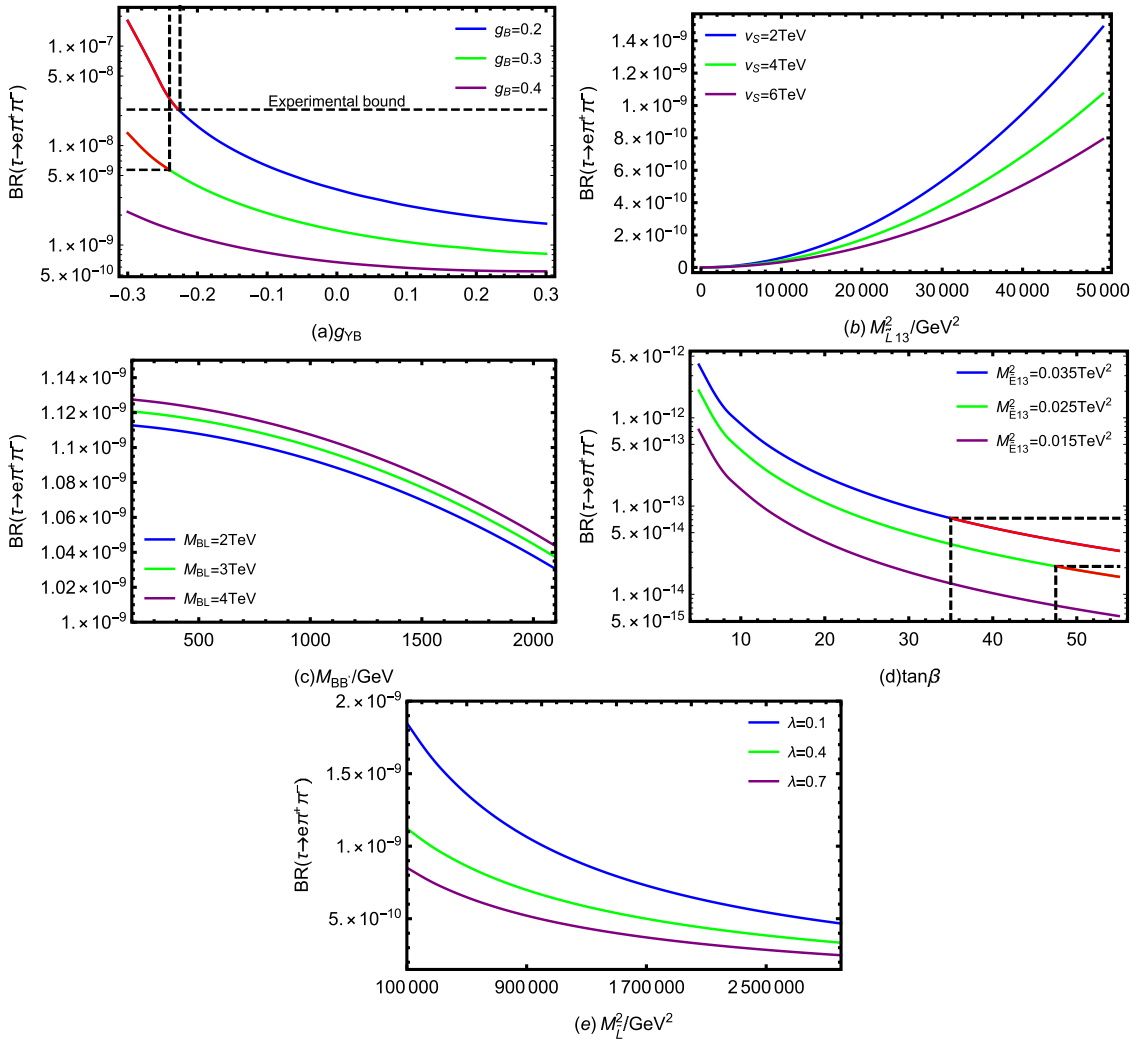

Fig. 5. (color online) Influence of various parameters on BR ($\tau \to e\pi^+\pi^-$).

trend is attributed mainly to the dual role of the two coupling constants on the NP effect. On one hand, both g_B and g_{YB} participate in the mass matrices and vertex structures of various SUSY particles, which can enhance LFV vertex coupling strengths. On the other hand, these two parameters simultaneously increase the mass of the particles and enhance the mass suppression effect of the loop propagator. The inhibition effect brought about by the improvement in mass significantly exceeds the amplitude increase caused by the coupling enhancement, resulting in the overall branching ratio decreasing as g_B and g_{YB} are increased. Therefore, g_B and g_{YB} can be regarded as sensitive and critical parameters.

In the case of $g_{YB} = 0.1$, $g_B = 0.3$, $\lambda = 0.4$, $\tan\beta = 25$, $M_{BB'} = 0.1$ TeV, $M_{BL} = 1$ TeV, $M_{\tilde{L}}^2 = 0.16$ TeV^2, Fig. 5(b) shows the trend of BR ($\tau \to e\pi^+\pi^-$) changing with $M_{\tilde{L}13}^2$. Each curve corresponds to different v_S values (the blue curve is for $v_S = 2$ TeV, the green curve is for $v_S = 4$ TeV, and the purple curve is for $v_S = 6$ TeV). $M_{\tilde{L}13}^2$ is an off-diagonal element in the left-handed slepton mass matrix. Its non-zero value introduces lepton flavor mixing between the first generation (e) and the third generation (τ). This flavor mixing makes flavor conservation less stringent, allowing LFV processes like $\tau \to e\pi^+\pi^-$ to occur. Therefore, the LFV effect is enhanced as $M_{\tilde{L}13}^2$ increases, causing the branching ratio to rise rapidly, and the three curves show obvious nonlinear positive growth. When the curves for the different v_S values are compared, it emerges that a larger v_S corresponds to a smaller branching ratio under the same $M_{\tilde{L}13}^2$ condition. v_S is the VEV of the Higgs singlet S and appears in almost all mass matrices involving spontaneous breaking of $U(1)_{B-L}$. In one-loop diagrams, the related particles participate in the propagation as internal propagators, which cause a significant propagation suppression effect when their masses increase with v_S, leading to a reduction in the branching ratio. In the numerical scan, it can be seen that the sensitivity of BR ($\tau \to e\pi^+\pi^-$) to $M_{\tilde{L}13}^2$ is much higher than that of v_S.

Assuming $g_{YB} = 0.1$, $g_B = 0.3$, $\lambda = 0.4$, $\tan\beta = 25$,

$v_S = 4$ TeV, $M^2_{\tilde{L}13} = 0.05$ TeV^2, $M^2_{\tilde{L}} = 0.16$ TeV^2, we show BR ($\tau \to e\pi^+\pi^-$) varying with $M_{BB'}$ via the blue curve ($M_{BL} = 2$ TeV), green curve ($M_{BL} = 3$ TeV), and purple curve ($M_{BL} = 4$ TeV) in Fig. 5(c). The parameter $M_{BB'}$ represents the mass of the $U(1)_Y$ and $U(1)_{B-L}$ gaugino mixing, whereas M_{BL} is the mass of the superpartner for the gauge boson under the $U(1)_{B-L}$ group. $M_{BB'}$ and M_{BL} are present in the mass matrix of the neutralino. Both of them affect the mixing and mass structure of the neutralino, thereby influencing the amplitude of the process in the Feynman diagrams involving the neutralino. As $M_{BB'}$ increases, the branching ratios of all curves decrease gradually. For any fixed $M_{BB'}$, a larger M_{BL} results in a slightly higher branching ratio. However, it can be seen from the variation of the vertical axis in Fig. 5(c) that the curves corresponding to the three different M_{BL} values are very close to each other, and that the range of changes in the vertical axis is relatively small. This indicates that both parameters do have an influence on the branching ratio; however, the overall contribution is weak and belongs to the secondary correction. Therefore, in the parameter sensitivity analysis of the process, the influence of $M_{BB'}$ and M_{BL} can be regarded as a mild regulatory effect rather than a decisive factor.

Under the conditions $g_{YB} = 0.1$, $g_B = 0.3$, $\lambda = 0.4$, $M_{BB'} = 0.1$ TeV, $M_{BL} = 1$ TeV, $v_S = 4$ TeV, $M^2_{\tilde{L}} = 0.16$ TeV^2, we study the relationship between BR ($\tau \to e\pi^+\pi^-$) and $\tan\beta$ in Fig. 5(d), where the curves are divided into three cases corresponding to $M^2_{\tilde{E}13} = 0.035$ TeV^2 (blue curve), $M^2_{\tilde{E}13} = 0.025$ TeV^2 (green curve), and $M^2_{\tilde{E}13} = 0.015$ TeV^2 (purple curve). The parameter $\tan\beta$ is defined as the ratio of the VEVs of the two Higgs doublets, namely $\tan\beta = v_u/v_d$. This parameter influences the vertex couplings and particle masses by directly affecting v_d and v_u. Because $\tan\beta$ appears in almost all the mass matrices of Fermions, scalars, and Majoranas, it must be a highly sensitive parameter. For each curve, the branching ratio decreases by about 2 to 3 orders of magnitude as $\tan\beta$ increases from 5 to 55. $M^2_{\tilde{E}13}$ denotes the flavor off-diagonal term between τ and e in the slepton softbreaking mass matrix, which essentially reflects the mixing strength among right-handed slepton SUSY particles. A larger $M^2_{\tilde{E}13}$ implies stronger lepton flavor mixing, which amplifies the loop contributions, leading to an upward shift in the overall branching ratio level. The right ends of the blue and green curves are marked in red, indicating that the corresponding parameter points have not exceeded the current experimental upper limit of $\tau \to e\pi^+\pi^-$, and thus, they have violated the constraint of $\tau \to e\gamma$. By contrast, the purple curve is allowed under both experimental limits because of its relatively low overall branching ratio.

Based on $g_{YB} = 0.1$, $g_B = 0.3$, $\tan\beta = 25$, $M_{BB'} = 0.1$ TeV, $M_{BL} = 1$ TeV, $v_S = 4$ TeV, $M^2_{\tilde{L}13} = 0.05$ TeV^2, Fig. 5(e) illustrates the trend of BR ($\tau \to e\pi^+\pi^-$) as $M^2_{\tilde{L}}$ varies, with three curves plotted corresponding to $\lambda = 0.1$ (blue curve), $\lambda = 0.4$ (green line), and $\lambda = 0.7$ (purple line). $M^2_{\tilde{L}}$ represents the diagonal term in the mass matrices of slepton as well as CP-even sneutrino and CP-old sneutrino, whose values affect the overall mass scale of the new physical particles involved in the loop process. With increases in $M^2_{\tilde{L}}$, the branching ratio shows a gradual downward trend. A higher $M^2_{\tilde{L}}$ signifies a greater mass of the relevant virtual particles, resulting in the significant suppression of the contribution of these particles in the low-energy process. In the superpotential, the term $\lambda\hat{S}\hat{H}_u\hat{H}_d$ involves the coupling constant λ. For a fixed $M^2_{\tilde{L}}$, a smaller λ value corresponds to a larger branching ratio. Although both have inhibitory effects on the branching ratio, based on the inclination of the curves in Fig. 5(e), BR ($\tau \to e\pi^+\pi^-$) is more sensitive to changes in $M^2_{\tilde{L}}$. This is because the variation of the branching ratio with $M^2_{\tilde{L}}$ under the same λ is much greater than the difference under different λ at a fixed $M^2_{\tilde{L}}$. This suggests that $M^2_{\tilde{L}}$ is a more critical parameter than λ in parameter constraints and sensitivity analysis.

B. Process of $\tau \to e\pi^+K^-$

To better explain how variables affect the branching ratio of ($\tau \to e\pi^+K^-$), we randomly scan the parameters. All the parameters involved are expressed in tabular form.

Supposing the parameters in conjunction with $T_\nu = 1$ TeV, $T_e = 1.5$ TeV, and $M^2_{\tilde{L}} = 0.16$ TeV^2, the relationship between g_B and $M^2_{\tilde{L}13}$ is shown in Fig. 6. Fig. 6 is plotted based on the parameters shown in Table 2. ◆ are distributed mainly in the lower area of Fig. 6, concentrated especially in the lower right corner. Within the range of $M^2_{\tilde{L}13} < 2\times10^4$ GeV^2, ◆ are the most densely distributed regardless of the value of g_B. ● are concentrated in the upper left part of Fig. 6 and are particularly dense in the region of $0.3 < g_B < 0.6$, 4×10^4 GeV$^2 < M^2_{\tilde{L}13} < 1\times10^5$

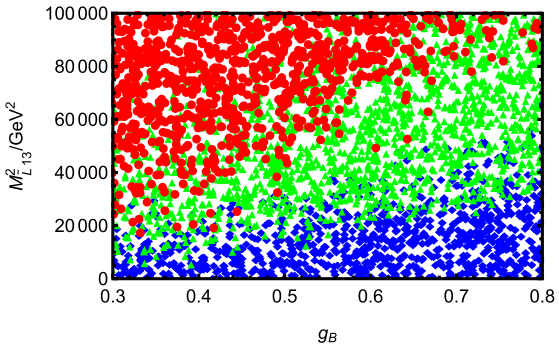

Fig. 6. (color online) Under the premises of current limits on LFV decays $\tau \to e\pi^+K^-$ and $\tau \to e\gamma$, reasonable parameter space in which to scatter points is selected. ◆ ($0 <$ BR ($\tau \to e\pi^+K^-$) $< 3\times10^{-11}$), ▲ ($3\times10^{-11} \le$ BR ($\tau \to e\pi^+K^-$) $< 3\times10^{-10}$), ● ($3\times10^{-10} \le$ BR ($\tau \to e\pi^+K^-$) $< 3.7\times10^{-8}$).

Table 2. Scanning parameters for Fig. 6.

Parameters	Min	Max
λ	0.05	0.4
λ_2	-0.3	-0.05
κ	0.01	0.7
g_{YB}	-0.4	0.2
g_B	0.3	0.8
$\tan\beta$	5	50
v_S/GeV	2000	7000
$M_{BB'}$/GeV	100	3000
M_{BL}/GeV	500	5000
$M^2_{\tilde{L}13}$/GeV^2	0	10^5
$M^2_{\tilde{E}}$/GeV^2	2×10^5	3×10^6

GeV^2, where there are basically no ◆ and ▲, indicating that most of the points in this parameter range correspond to larger branching ratios. ▲ are located between the ● and ◆ areas. ▲ gradually transition to the ● area toward the upper left and connect to the ◆ area toward the lower right, presenting a boundary structure along the diagonal direction. This distribution indicates that the two parameters have a significant joint effect on BR ($\tau \to e\pi^+K^-$), where the branching ratio tends to be larger for larger $M^2_{\tilde{L}13}$ and smaller g_B.

Next, we scatter points on $\tau \to e\pi^+K^-$ in Fig. 7 with the parameters in Table 3. Fig. 7(a) shows the distribution of BR ($\tau \to e\pi^+K^-$) as the parameters $M^2_{\tilde{L}13}$ and $M^2_{\tilde{E}}$ change. It can be observed that ◆, ▲, and ● uniformly cover the entire scanning interval in the $M^2_{\tilde{E}}$ direction, and that the trend of change is not significant, indicating that the impact of $M^2_{\tilde{E}}$ on the branching ratio is very small. In the direction of the horizontal axis, with the variation of $M^2_{\tilde{L}13}$, Fig. 7(a) shows an extremely obvious color partition. In the $M^2_{\tilde{L}13} < 20000\,\text{GeV}^2$ interval, almost all the data points are ◆, indicating that the branching ratio is in the lowest order of magnitude when this mixing parameter is relatively small. As $M^2_{\tilde{L}13}$ increases to the $2\times10^4\,\text{GeV}^2 \sim 6\times10^4\,\text{GeV}^2$ region, ▲ start to appear in large numbers, while ◆ decrease significantly, and the branching ratio rises rapidly to the middle order of magnitude. When $M^2_{\tilde{L}13} > 6\times10^4\,\text{GeV}^2$, ● become dominant, and ◆ and ▲ basically disappear, indicating that the branching ratio in this area is significantly enhanced and comes close to the experimental limit. The change in $M^2_{\tilde{L}13}$ is a sensitive factor determining the order-of-magnitude transition in branching ratio, which is consistent with what is reflected in Fig. 6.

Fig. 7(b) shows the change in BR ($\tau \to e\pi^+K^-$) with the parameters g_{YB} and $M^2_{\tilde{L}13}$. From the spatial distribution of the points, it can be observed that when g_{YB} takes a negative value, especially in the range of -0.4 to -0.1, and at the same time, $M^2_{\tilde{L}13}$ is relatively large ($M^2_{\tilde{L}13} > 6\times10^4\,\text{GeV}^2$), ● are the most concentrated, which indicates that the corresponding branching ratio is highest in this region. Conversely, the lower right corner of the graph is occupied mainly by ◆. In other words, the distribution of low branching ratios is densest when g_{YB} is close to the positive value (0 to 0.2) and $M^2_{\tilde{L}13}$ is smaller (less than $3\times10^4\,\text{GeV}^2$). Meanwhile, ▲ are located predominantly in the middle of Fig. 7(b), roughly forming a transition zone from the lower left to the upper right. Overall, the influence of $M^2_{\tilde{L}13}$ on the branching ratio is more direct, and changes in g_{YB} also have an obvious secondary effect. With increases in $M^2_{\tilde{L}13}$, the branching ratio gradually increases. Under the same $M^2_{\tilde{L}13}$, if g_{YB} is smaller, ● are also more likely to appear.

Under the conditions $\lambda = 0.4$, $\tan\beta = 25$, $T_\nu = 1$ TeV, $T_e = 1.5$ TeV, $v_S = 4$ TeV, $M_{BB'} = 0.1$ TeV, $M_{BL} = 1$ TeV, and $M^2_{\tilde{L}13} = 0.05\,\text{TeV}^2$, we plot g_B varying with $M^2_{\tilde{L}}$ in Fig. 8. These parameter ranges are given in Table 4. ● are concentrated mainly in the lower left part of Fig. 8, where $g_B < 0.5$ and $M^2_{\tilde{L}} < 1.5\times10^6\,\text{GeV}^2$. The points with a high branching ratio are more densely distributed, indicating that the parameter combination corresponding to this area is more likely to enhance the decay rate of $\tau \to e\pi^+K^-$. ▲

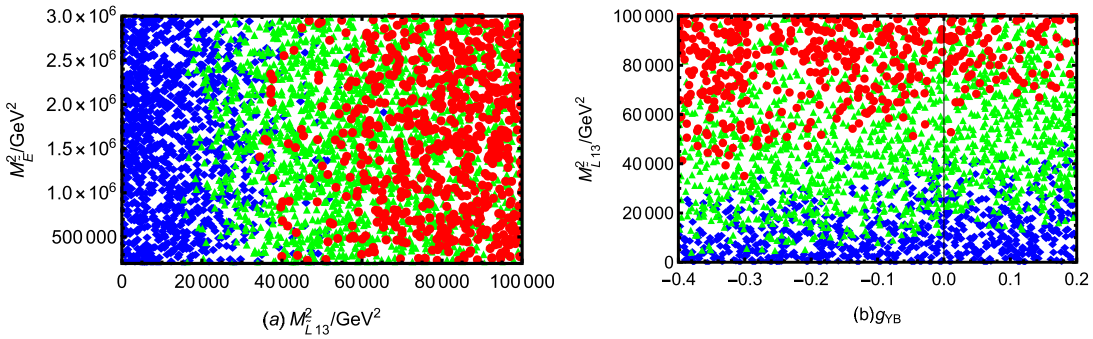

Fig. 7. (color online) Under the premises of current limits on LFV decays $\tau \to e\pi^+K^-$ and $\tau \to e\gamma$, reasonable parameter space in which to scatter points is selected. ◆ ($0 < \text{BR}(\tau \to e\pi^+K^-) < 3\times10^{-11}$), ▲ ($3\times10^{-11} \le \text{BR}(\tau \to e\pi^+K^-) < 3\times10^{-10}$), ● ($3\times10^{-10} \le \text{BR}(\tau \to e\pi^+K^-) < 3.7\times10^{-8}$)

Table 3. Scanning parameters for Fig. 7 and Fig. 10.

Parameters	Min	Max
λ	0.05	0.4
λ_2	-0.3	-0.05
κ	0.01	0.7
g_{YB}	-0.4	0.2
g_B	0.3	0.8
$\tan\beta$	5	50
v_S /GeV	2000	7000
$T_{\nu 13}$/GeV	-500	500
T_ν/GeV	-1500	1500
T_{e13}/GeV	-500	500
T_e/GeV	-2500	2500
$M_{BB'}$/GeV	100	3000
M_{BL}/GeV	500	5000
$M^2_{\tilde{L}13}$/GeV^2	0	10^5
$M^2_{\tilde{L}}$/GeV^2	1×10^5	3×10^6
$M^2_{\tilde{E}13}$/GeV^2	0	10^5
$M^2_{\tilde{E}}$/GeV^2	2×10^5	3×10^6

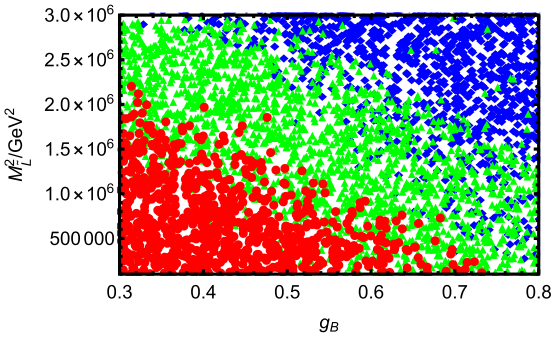

Fig. 8. (color online) Under the premises of current limits on LFV decays $\tau\to e\pi^+K^-$ and $\tau\to e\gamma$, reasonable parameter space in which to scatter points is selected. ◆ ($0<\mathrm{BR}(\tau\to e\pi^+K^-)<4\times10^{-11}$), ▲ ($4\times10^{-11}\le\mathrm{BR}(\tau\to e\pi^+K^-)<8\times10^{-11}$), ● ($8\times10^{-11}\le\mathrm{BR}(\tau\to e\pi^+K^-)<3.7\times10^{-8}$).

are distributed in a strip in the middle of Fig. 8, with a wide horizontal extension, indicating that this is the intermediate region, where the branching ratio transitions from high to low. Meanwhile, ◆ are distributed in large numbers in the upper right corner of Fig. 8. In the area of $g_B>0.6$ and $M^2_{\tilde{L}}>2\times10^6$ GeV^2, ● and ▲ have almost completely disappeared, and only ◆ remain, indicating that this parameter interval has a strong inhibitory effect on LFV decay. The dividing line shows a clear diagonal distribution, and the three regions of red, green, and blue basically transition from the bottom left to the top right. This shows that increasing either g_B or $M^2_{\tilde{L}}$ alone can reduce BR $(\tau\to e\pi^+K^-)$, and if both are increased at the same time, the inhibitory effect is more obvious. This diagram clearly reveals the sensitivity of the $\tau\to e\pi^+K^-$ decay process to the two parameters g_B and $M^2_{\tilde{L}}$, both of which play a key role in controlling the size of the branching ratio.

Table 4. Scanning parameters for Fig. 8.

Parameters	Min	Max
λ_2	-0.3	-0.05
κ	0.01	0.7
g_{YB}	-0.4	0.2
g_B	0.3	0.8
$M^2_{\tilde{L}}$/GeV^2	1×10^5	3×10^6
$M^2_{\tilde{E}}$/GeV^2	2×10^5	3×10^6

C. Process of $\tau\to eK^+K^-$

With the parameters $\kappa=0.1$, $g_{YB}=0.1$, $g_B=0.3$, $\lambda=0.4$, $\lambda_2=-0.25$, $\tan\beta=25$, $v_S=4$ TeV, $M_{BB'}=0.1$ TeV, $M_{BL}=1$ TeV, $M^2_{\tilde{L}13}=0.05$ TeV^2, $M^2_{\tilde{L}}=0.16$ TeV^2, $M^2_{\tilde{E}}=1.7$ TeV^2, we plot BR $(\tau\to eK^+K^-)$ schematic diagrams under the influence of different parameters, as shown in Fig. 9.

The trend of BR $(\tau\to eK^+K^-)$ with respect to T_{e13} is investigated in Fig. 9(a). Three lines are analyzed: a blue line for $T_e=2300$ GeV, a green line for $T_e=500$ GeV, and a purple line for $T_e=-1500$ GeV, demonstrating the sensitivity of the branching ratio to these parameters. All three curves show a monotonous upward trend. As T_{e13} changes from negative to positive, the branching ratio increases. The purple line is always at the top, the green line is in the middle, and the blue line is at the bottom. That is to say, under the same T_{e13} condition, the smaller the T_e, the larger the branching ratio. The spacing between the three lines slightly expands as T_{e13} increases. From a quantitative perspective, in the N-B-LSSM model, the mass square matrix of slepton is a 6×6 dimensional sturcture, which is determined jointly by the softbreaking mass term and the trilinear coupling term of the left-handed and right-handed three-generation lepton superparticles. The matrix can be split into 3×3 flavor subblocks, corresponding to the flavor-conserving and flavor-violating components, respectively. The parameter T_{e13} appears in the flavor-violating off-diagonal part of the matrix, while T_e corresponds to the flavor-conserving diagonal element. The flavor mixing is introduced in the diagonalization of slepton weak interaction eigenstates into the mass eigenstates, and the magnitude of the mixing angle is related to the ratio of off-diagonal element to a diagonal element $\frac{T_{e13}}{T_e}$. Therefore, the larger T_{e13} is, the smaller T_e is, and the BR $(\tau\to eK^+K^-)$ increases.

We study the effect of the parameter $T_{\nu 13}$ on BR $(\tau\to eK^+K^-)$ based on $T_\nu=1500$ GeV (blue line), $T_\nu=$

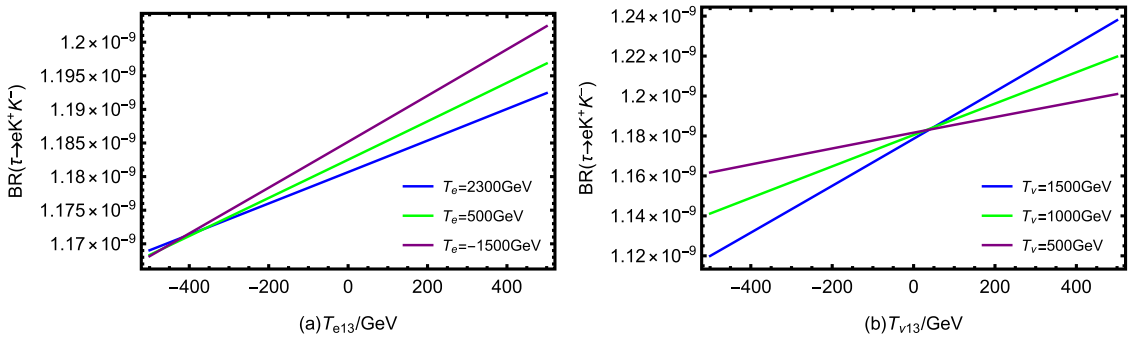

Fig. 9. (color online) Influence of various parameters on BR ($\tau \to eK^+K^-$): (a)T_ν = 1 TeV, (b) T_e = 1.5 TeV.

1000 GeV (green line), and $T_\nu = 500$ GeV (purple line), as shown in Fig. 9(b). $T_{\nu 13}$ represents the trilinear soft SUSY breaking term between the first and third generations in the CP-even and CP-odd sneutrino mass matrices, which is a lepton flavor-violating parameter. The branching ratio of the three curves increases with increases in $T_{\nu 13}$, and they intersect at $T_{\nu 13} = 0$ GeV. As $T_{\nu 13}$ moves away from the 0 point, the three curves gradually bifurcate. In the area of $T_{\nu 13} < 0$ GeV, the purple line is higher than the green line, which is higher than the blue line. The smaller the T_ν, the larger the branching ratio. In the region where $T_{\nu 13} > 0$ GeV, the order is reversed. The blue line is the highest, followed by the green line, and the purple line is the lowest. The larger the T_ν, the greater the branching ratio. This opposite sorting trend occurs because the positive or negative sign of $T_{\nu 13}$ affects the sign of the interference term when CP-even and CP-odd sneutrinos mix, thereby influencing the specific form of flavor mixing and changing the dependence direction of the branching ratio on T_ν.

It is worth noting that the range of the amount of relative change in the vertical axis of Fig. 9 is small. Therefore, it can be concluded that T_e, T_{e13}, T_ν, and $T_{\nu 13}$ do have an impact on BR ($\tau \to eK^+K^-$), but it is relatively small. This small variation shows that they are not the main parameters that control the process.

To better study LFV and find a reasonable parameter space for the $\tau \to eK^+K^-$ process, we study the effects of parameters κ, λ_2, $M^2_{\tilde{L}13}$, and $M^2_{\tilde{L}}$, and draw the scatter diagrams of a certain parameter space, as shown in Fig. 10. We scatter points according to the parameters given in Table 3 to obtain Fig. 10(a), (b), and (c).

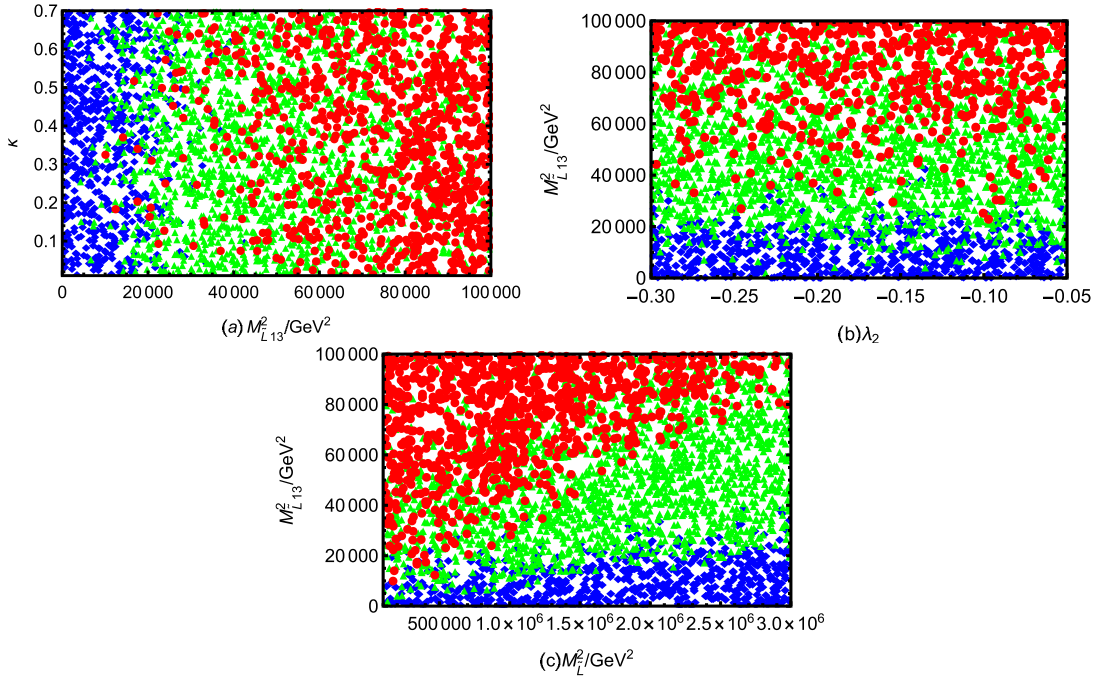

Fig. 10. (color online) Under the premises of current limits on LFV decays $\tau \to eK^+K^-$ and $\tau \to e\gamma$, reasonable parameter space in which to scatter points is selected. ◆ ($0 < \mathrm{BR}(\tau \to eK^+K^-) < 3\times10^{-11}$), ▲ ($3\times10^{-11} \le \mathrm{BR}(\tau \to eK^+K^-) < 5\times10^{-10}$), ● ($5\times10^{-10} \le \mathrm{BR}(\tau \to eK^+K^-) < 3.4\times10^{-8}$).

Table 5. Scanning parameters for Fig. 11.

Parameters	Min	Max
T_{e13}/GeV	–500	500
$T_{\nu 13}$/GeV	–500	500

In the study of the LFV process, the B-LSSM model has been widely investigated as an extension of the MSSM, and the additional $U(1)_{B-L}$ symmetry introduced has brought rich particle spectra and physical properties. The N-B-LSSM model used in this paper is structurally similar to the B-LSSM, but adds the new coupling terms and introduces several new parameters. Besides the parameter λ discussed in the previous subsection on $\tau \to e\pi^+\pi^-$, these parameters also include κ and λ_2, which do not exist in the traditional B-LSSM framework. Therefore, it is of great significance to study the numerical impact of these new parameters on the LFV process.

Fig. 10(a) and Fig. 10(b) show the distribution of BR$(\tau \to eK^+K^-)$ on the parameter plane $(M^2_{\tilde{L}13}, \kappa)$ and $(\lambda_2, M^2_{\tilde{L}13})$, respectively. Based on the overall distribution of the two diagrams, it can be observed that within the range of the selected parameters, the branching ratio increases with increases in $M^2_{\tilde{L}13}$. Whether in different processes or different diagrams, increases in $M^2_{\tilde{L}13}$ always lead to the rise of the branching ratio, demonstrating its crucial role as a source of flavor mixing. This unified trend further supports its dominant position in the LFV processes. Both κ (varying within the range of 0 to 0.7) and λ_2 (scanning between –0.3 and –0.05) have an even distribution of data points and do not show a clear trend. This suggests that BR $(\tau \to eK^+K^-)$ exhibits a moderate dependence on these two parameters, with the observed effects remaining relatively mild. κ is the parameter in the term $\frac{1}{3}\kappa\hat{S}\hat{S}\hat{S}$ of the superpotential. κ has a relation with the Higgs tree level potential and Higgs mass matrix through the mixing with Higgs singlet $\hat{S}$. λ_2 emerges in the term $\lambda_2\hat{S}\hat{\chi}_1\hat{\chi}_2$ of the superpotential. Because $\hat{\chi}_1$ and $\hat{\chi}_2$ are Higgs singlets, the term including λ_2 contributes to the CP-even Higgs mass squared matrix. The two parameters belong to the extended structure of the Higgs sector and do not directly appear in the vertices or intermediate state propagators of the $\tau \to eK^+K^-$ process. Consequently, it is difficult to significantly alter the amplitude of the process by changing these parameters, and thus, the branching ratio is insensitive to them.

Fig. 10(c) illustrates the variation of BR $(\tau \to eK^+K^-)$ in the two-dimensional parameter plane of $M^2_{\tilde{L}}$ and $M^2_{\tilde{L}13}$. ● are located mainly in the upper left part of the image, specifically in the area where $M^2_{\tilde{L}}$ is smaller and $M^2_{\tilde{L}13}$ is larger. In this region, the branching ratio is more likely to exceed 10^{-10}. ▲ are distributed predominantly in the middle zone, forming a transition band along the direction from bottom left to top right, showing an obvious oblique structure of the color boundary. Meanwhile, ◆ are clustered in the lower right corner area, indicating that the branching ratio is relatively small when $M^2_{\tilde{L}}$ is larger and $M^2_{\tilde{L}13}$ is smaller. As can be seen from Fig. 10(c), the branching ratio is significantly positively correlated with $M^2_{\tilde{L}13}$, whereas $M^2_{\tilde{L}}$ has a secondary but still important effect on BR $(\tau \to eK^+K^-)$, inhibiting the branching ratio.

To further investigate the effects of flavor-violating parameters on the LFV decay $\tau \to eK^+K^-$, we perform a detailed analysis of the dependence of the branching ratio on the trilinear couplings T_{e13} and $T_{\nu 13}$. In Fig. 11, the horizontal and vertical axes correspond to $T_{\nu 13}$ and T_{e13}, respectively. The markers indicate the predicted branching ratio BR $(\tau \to eK^+K^-)$ under the current experimental bounds (including BR $(\tau \to e\gamma)$ and BR $(\tau \to eK^+K^-)$). For better visualization, the points are categorized into three regions: ◆ $(0 < \text{BR}(\tau \to eK^+K^-) < 5\times10^{-14})$, ▲ $(5\times10^{-14} \le \text{BR}(\tau \to eK^+K^-) < 2\times10^{-13})$, and ● $(2\times10^{-13} \le \text{BR}(\tau \to eK^+K^-) < 3.4\times10^{-8})$. The red region corresponds to relatively large branching ratios, though still below the experimental upper bound.

From this figure, several important features can be observed. In the region where $T_{\nu 13} < 0$, for a fixed $T_{\nu 13}$, increasing T_{e13} significantly suppresses the branching ratio. Similarly, for a fixed T_{e13}, increasing $T_{\nu 13}$ also leads to a decrease in BR $(\tau \to eK^+K^-)$. This implies that in this region, both parameters act to suppress the LFV signal. In the region where $T_{\nu 13} > 0$, the behavior is opposite: increasing either T_{e13} or $T_{\nu 13}$ leads to a larger BR $(\tau \to eK^+K^-)$. This indicates a synergistic enhancement effect between the two parameters in this parameter space. The combination of these trends results in a clear diagonal pattern across the plot. Higher BR $(\tau \to eK^+K^-)$ values are located mainly toward the outer regions of the first and third quadrants, while lower BR $(\tau \to eK^+K^-)$ values concentrate near the middle region. This indicates that the influence of T_{e13} and $T_{\nu 13}$ depends not only on their abso-

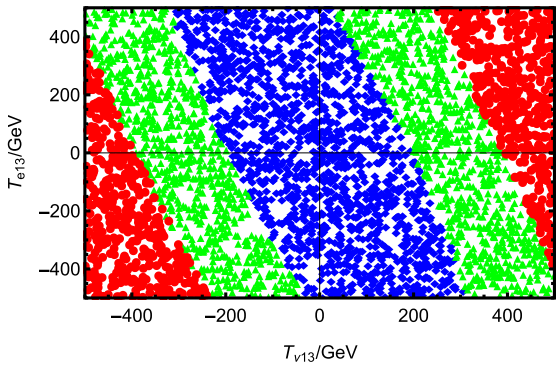

Fig. 11. (color online) Under the premises of current limits on LFV decays $\tau \to eK^+K^-$ and $\tau \to e\gamma$, reasonable parameter space in which to scatter points is selected. ◆ $(0 < \text{BR}(\tau \to eK^+K^-) < 5\times10^{-14})$, ▲ $(5\times10^{-14} \le \text{BR}(\tau \to eK^+K^-) < 2\times10^{-13})$, ● $(2\times10^{-13} \le \text{BR}(\tau \to eK^+K^-) < 3.4\times10^{-8})$.

Table 6. Scanning parameters for Fig. 12.

Parameters	Min	Max
$M_{\tilde{L}13}/\text{GeV}^2$	0	10^4
T_{e13}/GeV	-500	500

lute magnitudes but also significantly on their relative signs.

From a theoretical perspective, T_{e13} arises from trilinear soft SUSY breaking terms in the charged slepton sector, while $T_{\nu 13}$ affects the mass matrices of both CP-even and CP-odd sneutrinos. These parameters alter the flavor structure and mixing of sleptons and sneutrinos, thereby modulating the LFV transition amplitude. Depending on their values and signs, their contributions can interfere constructively or destructively, leading to the pattern observed in the figure.

Furthermore, although the dependence of BR $(\tau \to eK^+K^-)$ on T_{e13} and $T_{\nu 13}$ is clearly visible in the trend, the overall magnitude remains relatively small across most of the scanned parameter space. In particular, the majority of the parameter points yield BR $(\tau \to eK^+K^-)$ values in the range of 10^{-14} to 10^{-13}, significantly below the experimental limit of 3.4×10^{-8}. Only a small subset of points (mainly near the edges of the first and third quadrants) reach values greater than 2×10^{-13}. This suggests that whereas the influence of T_{e13} and $T_{\nu 13}$ on LFV is important, reaching experimental sensitivity also requires contributions from other parameters.

We include the contribution of $M^2_{\tilde{L}13}$ in Figs. 12, 13 and perform a combined analysis with T_{e13} and $T_{\nu 13}$. As shown in the figures, $M^2_{\tilde{L}13}$ exhibits the most direct and significant impact on the branching ratio. As this parameter increases from 0 GeV^2 to 10000 GeV^2, the markers of the scattered points transition from ◆ $(0 < \text{BR}(\tau \to eK^+K^-) < 6\times10^{-12})$ to ▲ $(6\times10^{-12} \le \text{BR}(\tau \to eK^+K^-) < 2.3\times10^{-11})$, and eventually to ● $(2.3\times10^{-11} \le \text{BR}(\tau \to eK^+K^-) < 3.4\times10^{-8})$. This indicates that BR $(\tau \to eK^+K^-)$ increases rapidly from the order of 10^{-12} to 10^{-11}, approaching the current experimental limit. This behavior reflects the strong enhancement effect of $M^2_{\tilde{L}13}$ on LFV processes. By contrast, the effects of $T_{\nu 13}$ and T_{e13} are relatively mild. Within the same range of $M^2_{\tilde{L}13}$, variations in either $T_{\nu 13}$ or T_{e13} can lead to some changes in BR $(\tau \to eK^+K^-)$, but the amplitude and trend are significantly less pronounced than those induced by $M^2_{\tilde{L}13}$. In particular, the influence of $T_{\nu 13}$ shows a more obvious directional tendency with a clearly sloped boundary, while the effect of T_{e13} appears more gentle.

This difference arises because $M^2_{\tilde{L}13}$ is the off-diagonal element in the left-handed slepton mass matrix, serving as a primary source of LFV. Because this parameter appears only in the mass term, its contribution to the branching ratio is monotonic and stable. Meanwhile, T_{e13}

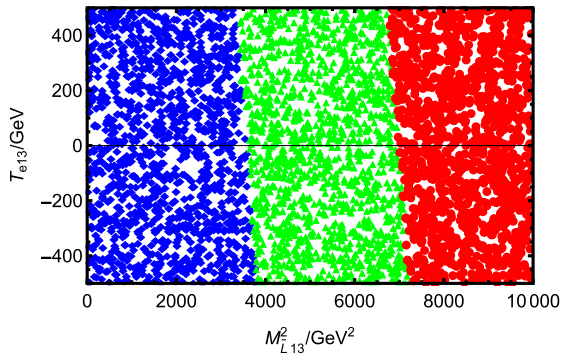

Fig. 12. (color online) Under the premises of current limits on LFV decays $\tau \to eK^+K^-$ and $\tau \to e\gamma$, reasonable parameter space in which to scatter points is selected. ◆ $(0 < \text{BR}(\tau \to eK^+K^-) < 6\times10^{-12})$, ▲ $(6\times10^{-12} \le \text{BR}(\tau \to eK^+K^-) < 2.3\times10^{-11})$, ● $(2.3\times10^{-11} \le \text{BR}(\tau \to eK^+K^-) < 3.4\times10^{-8})$.

Table 7. Scanning parameters for Fig. 13.

Parameters	Min	Max
$M_{\tilde{L}13}/\text{GeV}^2$	0	10^4
$T_{\nu 13}/\text{GeV}$	−500	500

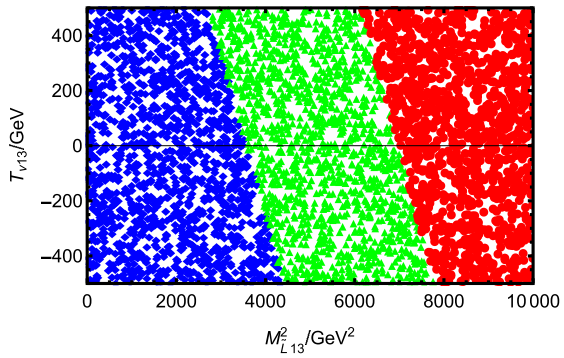

Fig. 13. (color online) Under the premises of current limits on LFV decays $\tau \to eK^+K^-$ and $\tau \to e\gamma$, reasonable parameter space in which to scatter points is selected. BR $(\tau \to eK^+K^-)$ ranges marked by ◆, ▲, ● are the same as in Fig. 12.

and $T_{\nu 13}$ act by introducing trilinear soft SUSY couplings between the third and first generations and modifying the off-diagonal structures of the slepton and sneutrino mass matrices, thereby affecting particle mixings and the LFV amplitudes. Their contributions are more indirect and nonlinear, leading to complex interference effects, yet generally limited in magnitude. These trends have already been analyzed in detail in Fig. 11.

V. DISCUSSION AND CONCLUSION

In this study, we analyze the LFV processes $\tau \to eM^+M^-$ ($\tau \to e\pi^+\pi^-$, $\tau \to e\pi^+K^-$, and $\tau \to eK^+K^-$) in the extended SUSY model N-B-LSSM. This model introduces right-handed neutrinos and three Higgs superfields

$\hat{\chi}_1$, $\hat{\chi}_2$, $\hat{S}$ with the local gauge group $SU(3)_C \otimes SU(2)_L \otimes U(1)_Y \otimes U(1)_{B-L}$, so that the rotation matrices and interaction vertices in the N-B-LSSM are richer than those in the MSSM. We construct the amplitude expressions of the corresponding processes based on the relevant Feynman diagrams.

With the upper limits on the branching ratio of $\tau \to e\gamma$ taken into account, many diagrams of numerical results are plotted after scanning large parameter spaces. The analysis of these numerical results reveals that g_B, g_{YB}, $\tan\beta$, $M_{\tilde{L}}^2$, $M_{\tilde{E}13}^2$, and $M_{\tilde{L}13}^2$ are sensitive parameters that have a significant impact on the branching ratios, whereas by comparison, λ, λ_2, κ, v_S, T_ν, $T_{\nu 13}$, T_e, T_{e13}, $M_{BB'}$, M_{BL}, and $M_{\tilde{E}}^2$ also affect the numerical results but not by a very large degree. In general, the non-diagonal elements corresponding to the initial and final leptons are the main sensitive parameters and LFV sources. We find that the order of magnitude of the $\tau \to eM^+M^-$ branching ratios can reach approximately $10^{-11} - 10^{-9}$. Most parameters can break the upper limit of the experiment and provide new ideas for finding NP.

APPENDIX A: REQUIRED WILSON COEFFICIENTS

In this section, we provide the concrete forms of the corresponding required Wilson coefficients as follows:

$$
\begin{aligned}
C_{VLR}^{eq} = & \sum_{F_1,F_2=\chi^\pm,\chi^\pm} \sum_{S_1,S_2=\tilde{\nu},\tilde{u}} -\frac{1}{2} I_9(x_{F_1},x_{F_2},x_{S_1},x_{S_2}) H_L^{S_1\tau\bar{F}_1} H_R^{S_1F_2\bar{e}} H_L^{S_2F_1\bar{d}} H_R^{S_2d\bar{F}_2} - \sum_{F_1,F_2=\chi^0,\chi^0} \sum_{S_1,S_2=\tilde{e},\tilde{q}} \frac{1}{2} \Big[I_9(x_{F_1},x_{F_2},x_{S_1},x_{S_2}) \\
& \times H_L^{S_1^*\tau\bar{F}_1} H_R^{S_1F_2\bar{e}} H_L^{S_2F_1\tilde{q}} H_R^{S_2^*q\bar{F}_2} - \frac{1}{2} I_8(x_{F_1},x_{F_2},x_{S_1},x_{S_2}) H_L^{S_1^*\tau\bar{F}_1} H_R^{S_1F_2\bar{e}} H_L^{S_2F_2\tilde{q}} H_R^{S_2^*q\bar{F}_1} \Big] + \sum_{F=\chi^0,\chi^\pm} \sum_{S=\tilde{e},\tilde{\nu}} \frac{1}{m_Z^2} \\
& \times \Big[\frac{1}{2} I_5(x_F,x_{S_1},x_{S_2}) [H_R^{S_2F\bar{e}} H_L^{S^*\tau\bar{F}} H^{ZS_1S_1^*} H_R^{\tilde{q}Zq} - H_R^{S_2F\bar{e}} H_R^{ZF_1\bar{F}_2} H_L^{S^*\tau\bar{F}_1} H_R^{\tilde{q}Zq}] + m_{F_1} m_{F_2} I_6(x_S,x_{F_2},x_{F_1}) \\
& \times H_R^{SF_2\bar{e}} H_L^{ZF_1\bar{F}_2} H_L^{S^*\tau\bar{F}_1} H_R^{\tilde{q}Zq} \Big] + \frac{1}{(m_e^2-m_\tau^2)} \Big[\frac{1}{2} I_1(x_F,x_S)(m_e^2-m_\tau^2) [\frac{Q_q e^2}{k^2} H_R^{S^*F\bar{e}} H_L^{S\tau\bar{F}} \\
& - \frac{1}{(k^2-m_Z^2)} H_R^{S^*F\bar{e}} H_L^{S\tau\bar{F}} H_L^{Z\tau\bar{e}} H_R^{\tilde{q}Zq}] + (m_e^2-m_\tau^2)[I_3(x_F,x_S) - I_4(x_F,x_S)] \times [\frac{Q_q e^2}{k^2} m_F (m_e H_L^{S^*F\bar{e}} H_L^{S\tau\bar{F}} \\
& + m_\tau H_R^{S^*F\bar{e}} H_R^{S\tau\bar{F}}) - \frac{1}{(k^2-m_Z^2)} \times m_F (m_e H_L^{S^*F\bar{e}} H_L^{S\tau\bar{F}} H_L^{Z\tau\bar{e}} H_R^{\tilde{q}Zq} + m_\tau H_R^{S^*F\bar{e}} H_R^{S\tau\bar{F}} H_L^{Z\tau\bar{e}} H_R^{\tilde{q}Zq})] \Big] \\
& + \sum_{F=\chi^0} \sum_{S=\tilde{e}} \frac{-Q_q e^2}{k^2} \Big[\frac{1}{2} I_1(x_F,x_S) H_R^{SF\bar{e}} H_L^{S^*\tau\bar{F}} + [I_2(x_F,x_S) - I_4(x_F,x_S)] \times [(m_\tau^2+m_e^2) H_R^{SF\bar{e}} H_L^{S^*\tau\bar{F}} \\
& + m_e m_\tau H_L^{SF\bar{e}} H_R^{S^*\tau\bar{F}}] + [I_2(x_F,x_S) - I_3(x_F,x_S)][m_F(m_e H_L^{SF\bar{e}} H_L^{S^*\tau\bar{F}} + m_\tau H_R^{SF\bar{e}} H_R^{S^*\tau\bar{F}})] \Big] \\
& + \sum_{F=\chi^\pm} \sum_{S=\tilde{\nu}} \frac{Q_q e^2}{k^2} \Big[[\frac{1}{2} I_1(x_F,x_S) - m_F^2 I_3(x_F,x_S)] H_R^{SF\bar{e}} H_L^{S^*\tau\bar{F}} + [2I_4(x_F,x_S) - I_2(x_F,x_S) - I_3(x_F,x_S)] \\
& \times [(m_\tau^2+m_e^2) H_R^{SF\bar{e}} H_L^{S^*\tau\bar{F}} + m_e m_\tau H_L^{SF\bar{e}} H_R^{S^*\tau\bar{F}}] + [I_4(x_F,x_S) - I_3(x_F,x_S)][m_F(m_e H_L^{SF\bar{e}} H_L^{S^*\tau\bar{F}} + m_\tau H_R^{SF\bar{e}} H_R^{S^*\tau\bar{F}})] \Big].
\end{aligned}
\tag{A1}
$$

$$
\begin{aligned}
C_{SRR}^{eq} = & \sum_{F_1,F_2=\chi^\pm,\chi^\pm} \sum_{S_1,S_2=\tilde{\nu},\tilde{u}} \frac{1}{8} I_9(x_{F_1},x_{F_2},x_{S_1},x_{S_2}) \Big[H_R^{S_1\tau\bar{F}_1} H_L^{S_1F_2\bar{e}} H_R^{S_2F_1\bar{d}} H_L^{S_2d\bar{F}_2} + H_L^{S_1\tau\bar{F}_1} H_R^{S_1F_2\bar{e}} H_L^{S_2F_1\bar{d}} H_R^{S_2d\bar{F}_2} \\
& + m_{F_1} m_{F_2} (H_L^{S_1\tau\bar{F}_1} H_L^{S_1F_2\bar{e}} H_L^{S_2F_1\bar{d}} H_L^{S_2d\bar{F}_2} - 3 H_R^{S_1\tau\bar{F}_1} H_R^{S_1F_2\bar{e}} H_R^{S_2F_1\bar{d}} H_R^{S_2d\bar{F}_2}) \Big] \\
& + \sum_{F_1,F_2=\chi^0,\chi^0} \sum_{S_1,S_2=\tilde{e},\tilde{q}} \frac{1}{8} I_9(x_{F_1},x_{F_2},x_{S_1},x_{S_2}) \Big[H_R^{S_1^*\tau\bar{F}_1} H_L^{S_1F_2\bar{e}} H_R^{S_2F_1\tilde{q}} H_L^{S_2^*q\bar{F}_2} + H_L^{S_1^*\tau\bar{F}_1} H_R^{S_1F_2\bar{e}} H_L^{S_2F_1\tilde{q}} H_R^{S_2^*q\bar{F}_2} \\
& - H_L^{S_1^*\tau\bar{F}_1} H_L^{S_1F_2\bar{e}} H_L^{S_2F_2\tilde{q}} H_L^{S_2^*q\bar{F}_1} - H_R^{S_1^*\tau\bar{F}_1} H_R^{S_1F_2\bar{e}} H_R^{S_2F_2\tilde{q}} H_R^{S_2^*q\bar{F}_1} - H_R^{S_1^*\tau\bar{F}_1} H_L^{S_1F_2\bar{e}} H_L^{S_2F_2\tilde{q}} H_R^{S_2^*q\bar{F}_1} \\
& - H_L^{S_1^*\tau\bar{F}_1} H_R^{S_1F_2\bar{e}} H_R^{S_2F_2\tilde{q}} H_L^{S_2^*q\bar{F}_1} + m_{F_1} m_{F_2} (H_L^{S_1^*\tau\bar{F}_1} H_L^{S_1F_2\bar{e}} H_L^{S_2F_1\tilde{q}} H_L^{S_2^*q\bar{F}_2} - 3 H_R^{S_1^*\tau\bar{F}_1} H_R^{S_1F_2\bar{e}} H_R^{S_2F_1\tilde{q}} H_R^{S_2^*q\bar{F}_2} \\
& + 4 H_R^{S_1^*\tau\bar{F}_1} H_R^{S_1F_2\bar{e}} H_R^{S_2F_2\tilde{q}} H_R^{S_2^*q\bar{F}_1}) \Big].
\end{aligned}
\tag{A2}
$$

$$
\begin{aligned}
C^{eq}_{SRL} = & \sum_{F_1,F_2=\chi^\pm,\mathcal{X}^\pm} \sum_{S_1,S_2=\bar{\nu},\tilde{u}} -\frac{1}{2} I_8(x_{F_1},x_{F_2},x_{S_1},x_{S_2}) H_R^{S_1\tau\bar{F}_1} H_R^{S_1F_2\bar{e}} H_L^{S_2F_1\bar{d}} H_L^{S_2d\bar{F}_2} - \frac{1}{8} I_9(x_{F_1},x_{F_2},x_{S_1},x_{S_2}) \\
& \times \Big[m_{F_1} m_{F_2} (H_L^{S_1\tau\bar{F}_1} H_L^{S_1F_2\bar{e}} H_L^{S_2F_1\bar{d}} H_L^{S_2d\bar{F}_2} + H_R^{S_1\tau\bar{F}_1} H_R^{S_1F_2\bar{e}} H_R^{S_2F_1\bar{d}} H_R^{S_2d\bar{F}_2}) + H_R^{S_1\tau\bar{F}_1} H_L^{S_1F_2\bar{e}} H_R^{S_2F_1\bar{d}} H_L^{S_2d\bar{F}_2} \\
& + H_L^{S_1\tau\bar{F}_1} H_R^{S_1F_2\bar{e}} H_L^{S_2F_1\bar{d}} H_R^{S_2d\bar{F}_2} \Big] - \sum_{F_1,F_2=\chi^0,\mathcal{X}^0} \sum_{S_1,S_2=\tilde{e},\tilde{q}} \frac{1}{2} I_8(x_{F_1},x_{F_2},x_{S_1},x_{S_2}) \Big[H_R^{S_1^*\tau\bar{F}_1} H_R^{S_1F_2\bar{e}} H_L^{S_2F_2\bar{q}} H_L^{S_2^*q\bar{F}_1} \\
& + H_R^{S_1^*\tau\bar{F}_1} H_R^{S_1F_2\bar{e}} H_L^{S_2F_1\bar{q}} H_L^{S_2^*q\bar{F}_2} \Big] + \frac{1}{8} I_9(x_{F_1},x_{F_2},x_{S_1},x_{S_2}) \times \Big[H_L^{S_1^*\tau\bar{F}_1} H_L^{S_1F_2\bar{e}} H_L^{S_2F_2\bar{q}} H_L^{S_2^*q\bar{F}_1} + H_R^{S_1^*\tau\bar{F}_1} H_R^{S_1F_2\bar{e}} H_R^{S_2F_2\bar{q}} H_R^{S_2^*q\bar{F}_1} \\
& + H_R^{S_1^*\tau\bar{F}_1} H_L^{S_1F_2\bar{e}} H_L^{S_2F_2\bar{q}} H_R^{S_2^*q\bar{F}_1} + H_L^{S_1^*\tau\bar{F}_1} H_R^{S_1F_2\bar{e}} H_R^{S_2F_2\bar{q}} H_L^{S_2^*q\bar{F}_1} - [m_{F_1} m_{F_2} (H_L^{S_1^*\tau\bar{F}_1} H_L^{S_1F_2\bar{e}} H_L^{S_2F_1\bar{q}} H_L^{S_2^*q\bar{F}_2} \\
& + H_R^{S_1^*\tau\bar{F}_1} H_R^{S_1F_2\bar{e}} H_R^{S_2F_1\bar{q}} H_R^{S_2^*q\bar{F}_2}) + H_R^{S_1^*\tau\bar{F}_1} H_L^{S_1F_2\bar{e}} H_R^{S_2F_1\bar{q}} H_L^{S_2^*q\bar{F}_2} + H_L^{S_1^*\tau\bar{F}_1} H_R^{S_1F_2\bar{e}} H_L^{S_2F_1\bar{q}} H_R^{S_2^*q\bar{F}_2}] \Big].
\end{aligned}
\tag{A3}
$$

$$
\begin{aligned}
C^{eq}_{TRR} = & \sum_{F_1,F_2=\chi^\pm,\mathcal{X}^\pm} \sum_{S_1,S_2=\bar{\nu},\tilde{u}} -\frac{m_{F_1} m_{F_2}}{8} I_9(x_{F_1},x_{F_2},x_{S_1},x_{S_2}) H_R^{S_1\tau\bar{F}_1} H_R^{S_1F_2\bar{e}} H_R^{S_2F_1\bar{d}} H_R^{S_2d\bar{F}_2} - \sum_{F_1,F_2=\chi^0,\mathcal{X}^0} \sum_{S_1,S_2=\tilde{e},\tilde{q}} \frac{1}{8} I_9(x_{F_1},x_{F_2},x_{S_1},x_{S_2}) \\
& \times \Big[H_R^{S_1^*\tau\bar{F}_1} H_R^{S_1F_2\bar{e}} H_R^{S_2F_2\bar{q}} H_R^{S_2^*q\bar{F}_1} + m_{F_1} m_{F_2} H_R^{S_1^*\tau\bar{F}_1} H_R^{S_1F_2\bar{e}} H_R^{S_2F_1\bar{q}} H_R^{S_2^*q\bar{F}_2} \Big].
\end{aligned}
\tag{A4}
$$

References

[1] S. Weinberg, Phys. Rev. Lett. **19**, 1264 (1967)
[2] A. Salam, Conf. Proc. C **680519**, 367 (1968)
[3] G. Aad *et al.* (ATLAS Coll.), Phys. Lett. B **716**, 1 (2012)
[4] S. Chatrchyan *et al.* (CMS Coll.), Phys. Lett. B **716**, 30 (2012)
[5] Y. Fukuda *et al.* (Super-Kamiokande Coll.), Phys. Rev. Lett. **81**, 1562 (1998)
[6] K. Abe *et al.* (T2K Coll.), Phys. Rev. Lett. **107**, 041801 (2011)
[7] J. Ahn *et al.* (RENO Coll.), Phys. Rev. Lett. **108**, 191802 (2012)
[8] F. An *et al.* (Daya Bay Coll.), Phys. Rev. Lett. **108**, 171803 (2012)
[9] H.P. Nilles, Phys. Rept. **110**, 1 (1984)
[10] H. E. Haber and G. L. Kane, Phys. Rept. **117**, 75 (1985)
[11] J. Rosiek, Phys. Rev. D **41**, 3464 (1990)
[12] X. Y. Han, S. M. Zhao, L. Ruan *et al.*, Eur. Phys. J. C **85**, 163 (2025)
[13] C. H. Chen, C. Q. Geng, Phys. Rev. D **74**, 035010 (2006)
[14] E. Arganda, M. J. Herrero, and J. Portoles, J. High Energy Phys. **06**, 079 (2008)
[15] A. Arhrib, R. Benbrik, and C. H. Chen, Phys. Rev. D **81**, 113003 (2010)
[16] A. Celis, V. Cirigliano, and E. Passemar, Phys. Rev. D **89**, 013008 (2014)
[17] F. Feruglio, P. Paradisi, and A. Pattori, Phys. Rev. Lett. **118**, 011801 (2017)
[18] T. Konno, PoS **2019**, 089 (2020)
[19] T. T. Wang, S. M. Zhao, X. X. Dong *et al.*, JHEP **04**, 122 (2022)
[20] R. Z. Sun, S. M. Zhao, M. Y. Liu *et al.*, arXiv: 2502.18130
[21] S. Navas *et al.* (Particle Data Group), Phys. Rev. D **110**, 030001 (2024)
[22] M. Carena, J. R. Espinosaos, C. E. M. Wagner, Phys. Lett. B **355**, 209 (1995)
[23] M. Carena, S. Gori, N. R. Shah *et al.*, JHEP **1203**, 014 (2012)
[24] G. Belanger, J. D. Silva, and H. M. Tran, Phys. Rev. D **95**, 115017 (2017)
[25] V. Barger, P. F. Perez, and S. Spinner, Phys. Rev. Lett. **102**, 181802 (2009)
[26] P. H. Chankowski, S. Pokorski, and J. Wagner, Eur. Phys. J. C **47**, 187 (2006)
[27] J. L. Yang, T. F. Feng, S. M. Zhao *et al.*, Eur. Phys. J. C **78**, 714 (2018)
[28] V. Cirigliano, K. Fuyuto, C. Lee *et al.*, JHEP **03**, 256 (2021)
[29] G. Aad *et al.* (ATLAS Coll.), Phys. Lett. B **796**, 68 (2019)
[30] G. Cacciapaglia, C. Csaki, G. Marandella *et al.*, Phys. Rev. D **74**, 033011 (2006)
[31] M. Carena, A. Daleo, B. A. Dobrescu *et al.*, Phys. Rev. D **70**, 093009 (2004)
[32] M. Endo, K. Hamaguchi, S. Iwamoto *et al.*, JHEP **07**, 075 (2021)
[33] M. Chakraborti, L. Roszkowski, and S. Trojanowski, JHEP **05**, 252 (2021)
[34] F. Wang, L. Wu, Y. Xiao *et al.*, Nucl. Phys. B. **970**, 115486 (2021)
[35] P. Cox, C. C. Han, and T. T. Yanagida, Phys. Rev. D. **104**, 075035 (2021)
[36] M. V. Beekveld, W. Beenakker, M. Schutten *et al.*, SciPost Phys. **11**, 049 (2021)
[37] M. Chakraborti, S. Heinemeyer, and I. Saha, Eur. Phys. J. C. **81**, 1114 (2021)
[38] P. Athron, C. Balazs, D. H. J. Jacob *et al.*, JHEP **09**, 080 (2021)
[39] L. Basso, Adv. High Energy Phys. **2015**, 980687 (2015)
[40] M. Drees, M. Gluck, and K. Grassie, Phys. Lett. B **157**, 164 (1985)
[41] U. Chattopadhyay, D. Das, and S. Mukherjee, JHEP **06**, 015 (2020)